# The Dynamical Core, Physical Parameterizations, and Basic Simulation Characteristics of the Atmospheric Component of the GFDL Global Coupled Model CM3

Leo J. Donner, Bruce L. Wyman, Richard S. Hemler, Larry W. Horowitz, *NOAA/GFDL, Princeton, New Jersey;* Yi Ming, Ming Zhao, *UCAR/GFDL, Princeton, New Jersey;* Jean-Christophe Golaz, Paul Ginoux, S.-J. Lin, M. Daniel Schwarzkopf, *NOAA/GFDL, Princeton, New Jersey;* John Austin, *UCAR/GFDL, Princeton, New Jersey;* Ghassan Alaka, *Colorado State University, Fort Collins, Colorado;* William F. Cooke, *High Performance Technologies, Inc./GFDL, Princeton, New Jersey;* Thomas L. Delworth, Stuart M. Freidenreich, C.T. Gordon, Stephen M. Griffies, Isaac M. Held, William J. Hurlin, *NOAA/GFDL, Princeton, New Jersey;* Stephen A. Klein, *Program for Climate Model Diagnosis and Intercomparison, Lawrence Livermore National Laboratory, Livermore, California;* Thomas R. Knutson, *NOAA/GFDL, Princeton, New Jersey;* Amy R. Langenhorst, Hyun-Chul Lee, *High Performance Technologies, Inc./GFDL, Princeton, New Jersey;* Yanluan Lin, *UCAR/GFDL, Princeton, New Jersey;* Brian I. Magi,Sergey L. Malyshev, *Princeton University/GFDL, Princeton, New Jersey;* Vaishali Naik, *High Performance Technologies, Inc./GFDL, Princeton, New Jersey;* Mary J. Nath, *NOAA/GFDL, Princeton, New Jersey;* Robert Pincus, *University of Colorado/ESRL, Boulder, Colorado;* Jeffrey J. Ploshay, V. Ramaswamy, Charles J. Seman, *NOAA/GFDL, Princeton, New Jersey;* Elena Shevliakova, *Princeton University/GFDL, Princeton, New Jersey;* Joseph J. Sirutis, William F. Stern, Ronald J. Stouffer, R. John Wilson, Michael Winton, Andrew T. Wittenberg, and Fanrong Zeng, *NOAA/GFDL, Princeton, New Jersey*

29 July 2010

For submission to *Journal of Climate*

*Corresponding Author Address:* Leo J. Donner, Geophysical Fluid Dynamics Laboratory/NOAA, Princeton University Forrestal Campus, 201 Forrestal Rd., Princeton, New Jersey 08540, leo.j.donner@noaa.gov

## ABSTRACT

The Geophysical Fluid Dynamics Laboratory (GFDL) has developed a coupled general circulation model (CM3) for atmosphere, oceans, land, and sea ice. The goal of CM3 is to address emerging issues in climate change, including aerosol-cloud interactions, chemistry-climate interactions, and coupling between the troposphere and stratosphere. The model is also designed to serve as the physical-system component of earth-system models and models for decadal prediction in the near-term future, for example, through improved simulations in tropical land precipitation relative to earlier-generation GFDL models. This paper describes the dynamical core, physical parameterizations, and basic simulation characteristics of the atmospheric component (AM3) of this model.

Relative to GFDL AM2, AM3 includes new treatments of deep and shallow cumulus convection, cloud-droplet activation by aerosols, sub-grid variability of stratiform vertical velocities for droplet activation, and atmospheric chemistry driven by emissions with advective, convective, and turbulent transport. AM3 employs a cubed-sphere implementation of a finite-volume dynamical core and is coupled to LM3, a new land model with eco-system dynamics and hydrology.

Most basic circulation features in AM3 are simulated as realistically, or more so, than in AM2. In particular, dry biases have been reduced over South America. In coupled mode, the simulation of Arctic sea ice concentration has improved. AM3 aerosol optical depths, scattering properties, and surface

clear-sky downward shortwave radiation are more realistic than in AM2. The simulation of marine stratocumulus decks remains problematic, as in AM2. The most intense 0.2% of precipitation rates occur less frequently in AM3 than observed.

The last two decades of the 20th century warm in CM3 by .32$^{O}$C relative to 1881-1920. The Climate Research Unit (CRU) and Goddard Institute for Space Studies analyses of observations show warming of .56$^{O}$C and .52$^{O}$C, respectively, over this period. CM3 includes anthropogenic cooling by aerosol-cloud interactions, and its warming by late 20th century is somewhat less realistic than in CM2.1, which warmed .66$^{O}$C but did not include aerosol-cloud interactions. The improved simulation of the direct aerosol effect (apparent in surface clear-sky downward radiation) in CM3 evidently acts in concert with its simulation of cloud-aerosol interactions to limit greenhouse gas warming in a way that is consistent with observed global temperature changes.

## 1. Introduction

The study of climate and climate change using general circulation models (GCMs) continues to advance rapidly, with impetus from widespread societal concern about anthropogenic and natural climate change, unprecedented global and field observational programs, and advances in theoretical and process-level understanding of atmospheric, oceanic, cryospheric, and terrestrial processes. The purpose of this paper is to describe recent development in the atmospheric component (AM3) of the Geophysical Fluid Dynamics Laboratory (GFDL) coupled model (CM3). AM3 is built upon the scientific and software framework of GFDL AM2 (Geophysical Fluid Dynamics Laboratory Global Atmospheric Model Development Team [GFDL GAMDT], 2004). Its major developmental thrusts were chosen to enable AM3 to address several key, emerging questions in climate and climate change that could not be addressed with AM2: (1) What are the roles of aerosol-cloud interactions, specifically, indirect effects of aerosols? (2) What are the dominant chemistry-climate interactions? AM3 development also aimed at enhanced capabilities for addressing emerging questions when coupled with bio-geochemical and ocean models: (1) What is the inter-play between climate and key bio-geochemical cycles? (2) To what extent is decadal prediction possible? The model also includes advances in the dynamical core, radiation, and other components.

Addressing these scientific questions implied particular approaches to AM3 development. In order to model aerosol-cloud interactions using a physically based treatment of aerosol activation, parameterizations for sub-grid variability of vertical velocity are important. This is because aerosol activation depends strongly on *local* vertical velocity, which, for both strati-form and convective clouds, can depart strongly from the large-scale average. AM3 parameterizes sub-grid vertical velocities for all clouds. In order to study chemistry-climate interactions, AM3 specifies chemical emissions and includes large-scale and convective transport, wet and dry removal, and key tropospheric and stratospheric reactions. AM3's stratospheric resolution has been increased, and its upper boundary has been raised, to treat stratospheric processes more comprehensively. AM3 itself does not include carbon, nitro-gen, or other bio-geochemical cycles, but particular attention has been given to improving its simulation of tropical precipitation, in order to enhance its usefulness as a component of earth-system models. AM3's improved strato-spheric resolution is also necessary for future research on phenomena such as the Southern Hemisphere Annular Mode, which likely plays a role in interan-nual variability important for decadal prediction (Thompson and Solomon, 2006).

Section 2 describes AM3's dynamical core. Section 3 presents its physical parameterizations, while Appendix 1 presents brief summaries of the land, ocean, and sea-ice models used with AM3 in CM3. Section 4 illustrates basic simulation characteristics of AM3 with prescribed sea surface temper-atures and in coupled mode. The inclusion of aerosol-cloud interactions in AM3 links cloud radiative properties to anthropogenic aerosols, whose optical properties and direct effects on shortwave radiation agree better with observations than in AM2. Section 4 shows that the overall impact of anthropogenic changes in trace gases and aerosols is consistent with observed global surface temperature changes.

## 2. Dynamical Core

As in CM2.1 (Delworth et al. 2006), the dynamical core used in AM3/CM3 follows the finite-volume algorithms described in Lin and Rood (1996, 1997) and Lin (1997, 2004), with the following major modifications.

In an effort to enhance the model's parallel computing efficiency and to improve simulation quality in polar regions, the dynamical core formulated on, and optimized specifically for, the latitude-longitude grid has been significantly modified to use a general curvilinear coordinate system. The non-orthogonal gnomonic projection in the general cubed-sphere geometry described by Putman and Lin (2007) is chosen due to its excellent grid uniformity and better overall accuracy. The use of the non-orthogonal coordinate system necessitated major changes to the transport operators (Putman and Lin, 2007) and the need to compute both the co- and contra-variant wind components (e.g., Sadourny, 1972).

Compared to the original latitude-longitude grid formulation, the use of the cubed-sphere grid in the new finite-volume core greatly improved the computational efficiency due to two major algorithmic modifications. First, the flux-form semi-Lagrangian extension (Lin and Rood, 1996) needed to stabilize the (large-time-step) transport processes near the poles is no longer needed with the use of the cubed-sphere grid. Second, and related to the first, the polar Fourier filtering required for the stabilization of the fast waves is also no longer needed. Both modifications led to greatly improved computation and communication load balancing, enabling the efficient use of 2D domain decomposition on each of the six faces of the cube.

The model's horizontal resolution is denoted as Cn, where n is an integer number indicating total number of cells (finite volumes) along each edge of the cube. In AM3, the model's resolution is C48. The total number of cells on the sphere is therefore 6x48x48=13,824, and the size of the grid cell varies from 163 km (at the 6 corners of the cubed sphere) to 231 km (near the center of each face). The C48 resolution model scales roughly an order of magnitude better (can use 864, versus 30, central processing units) than its latitude-longitude counterpart (2x2.5 degrees resolution) used in CM2.1, enabling nearly the full use of GFDL 1024-core SGI Altix-3000 system.

The vertical co-ordinate in AM3 follows Simmons and Burridge (1981), but the number of layers has been increased to 48 (from 24 layers in AM2). The uppermost level in AM3 has a pressure of 1 Pa, a height of about 86 km for a surface pressure of 1013.25 hPa and scale height of 7.5 km (equivalently, isothermal with a temperature of approximately 256.2 K), compared to around 35 km in AM2. The augmentation in vertical levels is aimed at resolving the stratosphere sufficiently well that its basic chemical and dynamical processes can be reasonably simulated. Table 1 shows the positions of the intermediate levels, which bound AM3's layers.

## 3. Physical Parameterizations

### *a. Radiation*

The basic shortwave and longwave radiation algorithms are described in Freidenreich and Ramaswamy (1999) and Schwarzkopf and Ramaswamy (1999), respectively, modified as in GFDL GAMDT (2004). The solar constant is from the Total Irradiance Monitor (Kopp et al., 2005), as recommended for Climate Model Intercomparison 5 (http://www.geo.fu-berlin.de/en/met/ag/strat/forschung/ SOLARIS/Input_data/CMIP5_solar_irradiance.html).

#### 1) SUB-GRID VARIABILITY AND OVERLAP

All-sky radiative transfer calculations account for the effect of clouds using the Monte Carlo Independent Column Approximation (Pincus et al., 2003), which treats variability by creating a set of sub-columns consistent with cloud properties (including variability) and vertical structure (i.e., overlap). The in-cloud distribution of ice and water content in stratiform clouds is diagnosed from the cloud fraction and condensate amount (Pincus et al., 2006), and vertical structure assumes that the rank correlation of total water falls off exponentially with the distance between layers using a scale height of 1 km (Pincus et al., 2005). These formulations differ from those in AM2 and allow cloud optical properties to be used as predicted, rather than being arbitrarily multiplied by 0.85 as in AM2. The radiative properties of shallow and deep convective clouds (Section 3e) are also included. Convective clouds are assumed to be internally homogeneous and to obey maximum overlap. When convective clouds occur in a sub-column they replace any stratiform clouds in layers where both clouds occur, which slightly decreases the overall stratiform cloud amount.

Effective radius in each sub-column is computed assuming that the predicted cloud drop number is uniform for each cloud type within each large-scale column. In stratiform clouds and shallow cumulus, drop size depends on aerosol activation, as described in Section 3f.

2) CLOUD OPTICS

The sizes of cloud droplets in stratiform and shallow cumulus clouds depend on aerosol activation and are determined using the procedures described in Section 3f. In deep cumulus updraft cells, the sizes of liquid droplets follow Bower et al. (1994). Size-dependent shortwave optical properties for cloud liquid follow Slingo (1989). Longwave liquid optical properties follow Held et al. (1993) and depend on water path but not particle size. AM3 does not link ice nucleation to crystal sizes. In shallow cumulus and stratiform ice clouds, ice particle sizes are diagnosed as a function of temperature, based on aircraft observations (Donner et al., 1997) with radiative properties following Fu and Liou (1993). In mesoscale updrafts associated with deep convection, ice crystals increase in size with distance from the top of updraft as in McFarquhar et al. (1999), except that McFarquhar et al.'s (1999) heights are replaced with equivalent normalized fractional distances between the top and base of the mesoscale updraft. Ice crystals in cumulus cell updrafts are assigned a generalized effective size of 18.6 $\mu$m, a value noted by Fu (1996) from the early temporal evolution (most likely dominated by deep cells) of a convective system in the Central Equatorial Pacific Experiment. Solar and infrared radiative properties of ice crystals in cell updrafts and mesoscale anvils are obtained from Fu (1996) and Fu et al. (1998), respectively.

#### 3) GAS CONCENTRATIONS

Historical concentrations of carbon dioxide, nitrous oxide, methane and halocarbons (CFC-11, CFC-12, CFC-113, and HCFC-22) are obtained from www.iiasa.ac.at/web-apps/tnt/RcpDb/, where the Representative Concentration Pathways may also be found. Note that the methane specification for radiation differs from the methane obtained from the chemistry calculations described in Section 3g. Tropospheric and stratospheric ozone are modeled as described in Section 3g.

#### 4)AEROSOL OPTICS

The effects of volcanoes are included in the AM3 and CM3 simulations described in Section 4. Sulfur-dioxide emissions from volcanoes are described in Section 3f. Direct injection of sulfur into the stratosphere from volcanic eruptions is not included, nor is carbonyl-sulfide chemistry, a major source of background stratospheric aerosol. To compensate, in the stratosphere, a time series of volcanic optical properties is specified as in Stenchikov et al.

(2006).

Aerosol optical properties (i.e., extinction efficiency, single-scattering albedo and asymmetry factor) are based on Mie theory, assuming all particles spherical. Log-normal size distribution is assumed for sulfate and carbonaceous aerosols. The geometric mean radius and standard deviation of the log-normal distribution for sulfate and black carbon are from Haywood and Ramaswamy (1998), and for organics from Hess et al. (1998). The mass size distribution of dust and sea-salt is assumed constant within five bins from 0.1 to 10 $\mu$m. Hygroscopic growth is considered for sulfate, sea-salt, and aged (hydrophilic) organic carbon. We model the hygroscopic growth of sulfate after that of pure ammonium sulfate (Tang and Munkelwitz, 1994), of sea-salt as pure sodium chloride (Tang et al., 1997), and of hydrophilic organics as a mixture of acids and insoluble organics (Ming et al., 2005). The refractive indices of sulfate and black carbon are from Haywood and Ramaswamy (1998), of organics from Hess et al. (1998), sea salt from Tang et al. (1997), and dust from Balkanski et al. (2007) assuming 2.7% content of hematite. Internal mixture of sulfate and aged (hydrophilic) black carbon is calculated by volume weighted average of their refractive index. All other aerosols are assumed externally mixed.

### *b. Gravity Wave Drag*

Orographic gravity wave drag is parameterized using Stern and Pierrehumbert (1988), as described in GFDL GAMDT (2004). Non-orographic gravity-wave drag is parameterized using Alexander and Dunkerton (1999), which treats vertical propagation of wave components of a spectrum of gravity waves with a range of phase speeds and horizontal waves, assuming that the momentum associated with each wave component is deposited locally at the level of linear wave breaking. There are uncertainties in the seasonal, latitudinal, and height dependencies of gravity-wave sources and sinks. Alexander and Rosenlof (2003) found that parameters related to the sources and sinks varied from the tropics to the extra-tropics. In the AM3 application of Alexander and Dunkerton (1999), the momentum source is represented by a broad spectrum of wave speeds (half-width of 40 m $s^{-1}$) with a resolution of 2 m $s^{-1}$and a single horizontal wavelength of 300 km. The amplitude of the momentum source is 0.005 Pa in the northern middle and high latitudes, 0.004 Pa in the tropics, and 0.003 Pa in the southern middle and high latitudes, with smooth transitions around $30^{O}$ N and S. The asymmetry in the northern and southern sources improves the simulation of stratospheric zonal winds and polar temperatures. The wave launch height decreases smoothly from 350 hPa at the equator to near the surface at the poles. Optimizing the input parameters was eased by limiting the influence of the orographic wave drag parameterization to below 30 hPa. The scheme yields a reasonable semi-annual oscillation. However, the vertical resolution employed here is not sufficiently fine to enable simulation of the quasi-biennial oscillation (Giorgetta et al., 2006).

### c. *Turbulence and Planetary Boundary Layer*

Turbulence and planetary boundary layers (PBLs) in AM3 are treated as in AM2. Lock et al. (2000) is used for convective PBLs and stratocumulus layers. Louis (1979) is employed for other unstable layers. Stability functions with thresholds dependent on Richardson number are adopted for stable layers. Variations in vertical diffusion coefficients are damped. Full details can be found in GFDL GAMDT (2004).

### d. *Stratiform Clouds*

Cloud fraction, liquid, and ice in AM3 are prognosed based on Tiedtke (1993), with modifications mostly as described in GFDL GAMDT (2004). Detrainment of cloud liquid, cloud ice, and cloud fraction are treated slightly differently than in GFDL GAMDT (2004) to be consistent with the Donner et al. (2001) deep and Bretherton et al. (2004) shallow cumulus parameterizations in AM3. Denoting the mixing ratio of liquid or ice or the cloud fraction by $X$, its stratiform tendency due to deep convection is

$$gD_{meso}X_{meso} - g\frac{\partial(M_{deep}\overline{X})}{\partial p}. \tag{1}$$

Here, $D_{meso}$ is the rate of change with pressure of the mass flux in the detraining layers of mesoscale updrafts in convective systems. The sum of upward mass fluxes in deep cells and mesoscale updrafts, reduced by the downward mass fluxes in mesoscale downdrafts, is $M_{deep}$, while $g$ and $p$ denote the gravity constant and pressure, respectively. An overbar denotes a large-scale average. Detrainment from deep convective cells in Donner et al. (2001) is directed to the mesoscale circulations, which are part of the cumulus parameterization. Thus, detrainment into the stratiform clouds is from the mesoscale updrafts only.

The corresponding stratiform tendency due to shallow cumulus is

$$gD_{shal}(X^* - \overline{X}) - gM_{shal}\frac{\partial \overline{X}}{\partial p}, \tag{2}$$

where $X^*$ denotes a property within shallow cumulus.

Microphysical processes, except for activation of liquid cloud drops (described in Section 3f), follow Rotstayn (1997) and Rotstayn et al. (2000), as described in GFDL GAMDT (2004). The number of activated aerosols depends on aerosol mass, composition, and vertical velocity. To account for the effect of sub-grid variability, the vertical velocity is assumed to be normally distributed within each model grid box and the activation computed by integration over this distribution following Ghan et al. (1997). The mean of the distribution is the velocity driving the stratiform condensation in the Tiedtke (1993) parameterization, and the variance is related to the turbulence mixing coefficients. A minimum variance of 0.7 m $s^{-1}$is imposed. The integration is performed numerically using a 64-point Gauss-Hermite quadrature. Through it's control on aerosol activation, sub-grid variability in vertical velocity is a major factor in the magnitude of aerosol indirect effects (Golaz et al., 2010).

Finally, several parameters in the Tiedtke (1993) parameterization have been altered from their GFDL GAMDT (2004) values. The critical droplet radius for autoconversion is 8.2 $\mu$m. The erosion constants when vertical diffusion is active, when convection (shallow, deep, or both) is active without vertical diffusion, and when neither convection nor diffusion is active are $7 \times 10^{-5}$ s$^{-1}$, $7 \times 10^{-5}$ s$^{-1}$, and $1.3 \times 10^{-6}$ s$^{-1}$, respectively. The ice fall speeds follow Heymsfield and Donner (1990), multiplied by a factor of 1.5. These changes are regarded as within observational or conceptual uncertainties, given the design of the parameterizations. The changes were chosen to increase realism of the simulations, particularly with regard to radiation balance, precipitation, and implied ocean heat transports in AM3 integrations with prescribed sea surface temperatures (SSTs).

### *e. Cumulus Convection*

Deep cumulus systems consist of deep updraft cells, mesoscale updrafts, and mesoscale downdrafts (Donner, 1993; Donner et al., 2001; Wilcox and Donner, 2007). Several modifications have been made in AM3 for computational efficiency or simulation improvement. The plumes in the deep updraft cells are discretized on the AM3 vertical grid instead of a higher-resolution cloud grid. With the coarser plume resolution, entrainment coefficients have been increased relative to those in Donner (1993) by a factor of 1.45. Liquid/frozen-water static energy (conservative without precipitation) is used instead of temperature for plume thermodynamics. Aspects of the water budget in deep convective systems related to $R_m$, precipitation from mesoscale updrafts; $E_{me}$, condensate transfer from mesoscale updrafts to large-scale stratiform clouds (cf., Section 3d); $C_{mu}$, condensation and deposition in mesoscale updrafts; and $C_A$, lateral transfer of condensate from deep updraft cells to mesoscale updrafts, have been modified. In particular, $\frac{R_m}{C_{mu}+C_A}$ and $\frac{E_{me}}{C_{mu}+C_A}$ are 0.55 and 0.05, respectively, compared to 0.50 and 0.10 in Donner (1993). In AM3, 10% of the condensate in the cell updrafts at the detrainment level evaporates, while all remaining condensate that does not fall from the cell updrafts as precipitation is transferred to the mesoscale updraft. In Donner (1993), 13% of the condensate in the cell updrafts that is not removed as precipitation evaporates near the detrainment level, while 25% evaporates in cell-scale downdrafts and 62% is transferred to the mesoscale updraft. The Donner (1993) partitionings are based on observations reported by Leary and Houze (1980). In AM3, the top of the mesoscale circulation is specified as the level of zero buoyancy (or at a pressure 10 hPa less than the level of zero buoyancy, if the deepest cell top is above the level of zero buoyancy due to overshooting). The top of mesoscale circulation is restricted to be no higher than the temperature minimum corresponding to the local tropopause. The latter condition was found to be necessary to prevent excessive water vapor in the stratosphere.

The closure for deep cumulus results in heating by cumulus convection relaxing convective available potential energy (CAPE) toward a threshold over a relaxation time scale (cf., Eq. (2) in Wilcox and Donner (2007)). The CAPE threshold is 1,000 J kg$^{-1}$, and the relaxation time scale is 8 hrs.

Shallow cumulus follows Bretherton et al. (2004), modified as in Zhao et al. (2009), with the empirical non-dimensional parameter controlling the strength of the lateral mixing ($c_0$ in Eq.(18) in Bretherton et al. (2004)) set to 13.5.

Both deep and shallow cumulus diffuse large-scale horizontal momentum in proportion to their mass fluxes, as in GFDL GAMDT (2004). The non-dimensional constant $\gamma$ in Eq. (1) of GFDL GAMDT (2004), which is a factor with the cumulus mass flux in the term added to the vertical diffusion coefficient, takes the value 0.26 in AM3. The GFDL GAMDT (2004) value is 0.20.

Finally, moist adiabatic adjustment (MAA) (Manabe et al., 1965) has been retained, since a saturated atmosphere at grid scale should not be unstable or moist beyond saturation. The parameterizations for deep and shallow cumulus do not preclude these conditions, which produce small amounts of precipitation relative to other sources.

The changes in the parameter settings for deep and shallow convection are within observational uncertainty and, as with the stratiform parameter settings discussed in Section 3d, resulted in improved realism in key aspects of the atmospheric circulation important for coupled climate modeling, e.g., implied ocean heat transports.

In the AM3 integration described in Section 4a, deep convective cells dominate in the middle and upper troposphere in the tropics, but at pressures of 100 to 200 hPa, the mass fluxes in mesoscale updrafts are comparable to those in the cells (Fig. 1). Mesoscale downdrafts have the smallest mass fluxes among the convective components, but can extend to the PBL, where changes by these downdrafts in thermodynamic and moisture structure can impact surface fluxes. Shallow cumulus can co-exist with deep convection, and, though its vertical extent is not imposed, generally is confined below about 500 hPa. Deep convection can only occur when the level of zero buoyancy is at a pressure less than 500 hPa. Both are called from the same atmospheric state. In AM3, deep convective precipitation dominates in the tropics, while stratiform precipitation prevails in the middle latitudes (Fig. 2a). The small values of precipitation associated with MAA indicate that the other precipitation parameterizations generally preclude the development of over-saturated, unstable conditions. The mid-latitude maxima in precipitation from the MAA coincide with the edges of the faces of the cubed-sphere in the dynamical core. Relative to precipitation reported by the Version-2 Global Precipitation Climatology Project (GPCP v.2) (Adler et al., 2003), AM3 produces 16% excessive precipitation. In CM3, described in Section 4, sea-surface temperatures depart from the observed values specified in the AM3 integrations when AM3 is coupled to ocean and sea-ice models, with appreciable effects on precipitation patterns (Fig. 2b). Most notably, a double inter-tropical convergence zone (ITCZ), not evident in GPCP v.2, is apparent. This double maxima occurs in all of the parameterized sources of precipitation, despite wide variations in the ways in which occurrence of precipitation in these parameterizations is related to large-scale flows. The departure of CM3 precipitation patterns from AM3 patterns is typical when coupling atmospheric and oceanic GCMs and is evidently a consequence of a chain of interactions between the ocean and atmosphere components (e.g., Zhang et al., 2007).

### *f. Aerosols*

AM3 calculates the mass distribution and optical properties of aerosols based on their emission, chemical production, transport, and dry and wet removal. The transport processes include advection, convection, and eddy diffusion by turbulence. The chemical production of sulfate includes gas and aqueous-phase oxidation of sulfur dioxide by radicals, ozone, and hydrogen peroxide, which are calculated explicitly by the chemical mechanism described in Section 3g. Dry deposition includes gravitational settling and impaction at the surface by turbulence. Wet deposition takes into account in- and below-cloud scavenging by large-scale and convective clouds.

Anthropogenic and biomass burning emissions of sulfur dioxide, black carbon, and organic carbon are from Lamarque et al. (2010). Dimethyl sulfide (DMS) emission is calculated using an empirical formula as a function of seawater DMS concentration and wind speed at 10 m, as described by Chin et al. (2002).

Secondary organic aerosols are produced by terrestrial and oceanic sources. Terrestrial production includes natural and anthropogenic sources. The natural source includes oxidation of terpenes emitted from plants, which yields particulate organics (Dentener et al., 2006). The yield factor varies from 0.11 per molecule at latitudes lower than $20^{O}$ to 0.55 per molecule at the poles. The anthropogenic source follows Tie et al. (2005), where 10% of the butane oxidized by hydroxyl radicals becomes particulate organics. The oceanic source is O'Dowd et al.'s (2008) organic sea-spray source function. Anthropogenic and natural secondary organic aerosol production is 11.3 and 31.5 Tg $yr^{-1}$, respectively.

Dust emission follows the parameterization by Ginoux et al. (2001) and is based on the preferential location of sources in topographic depressions. Sea salt particles are emitted from the ocean according to Monahan et al. (1986).

For volcanoes, time-invariant sulfur dioxide emissions are specified to be the total *sulfur* emissions recommended by AeroCom (Dentener et al., 2006) for continuous degassing and (time-averaged) explosive emissions, multiplied by a factor of 0.25. These emissions are injected 500 to 1500 m above volcano tops for explosive emissions and over the upper third of volcanoes for continuously degassing volcanoes and are thus confined to the troposphere. The factor applied is justified by the need to scale the total sulfur emissions to include only sulfur dioxide emissions and to simulate realistic sulfur dioxide and sulfate abundances in otherwise clean regions with volcano sources, noting that considerable uncertainty exists in volcano emissions. Due to the absence of some chemical processes important for the formation of stratospheric volcanic aerosols, e.g., related to carbonyl sulfide, and the absence of direct injection of volcanic aerosols into the stratosphere, a stratospheric signature for volcanoes is imposed through the specification of a time series of spatial distributions of optical properties, as noted in Section 3a.

Following Cooke et al. (1999), we assume that 80% of black carbon and 50% of organics emitted are hydrophobic, the rest being hydrophilic. Hydrophobic black carbon and organic aerosols undergo aging processes to become hydrophilic with e-folding times of 1.44 and 2.88 days, respectively. Secondary organic aerosols are treated as hydrophilic.

Chemical processes related to aerosol formation are discussed in Section 3g. Aerosols are removed by dry deposition at the surface and by scavenging in stratiform and convective clouds. Dry deposition velocities for aerosols are calculated interactively using a wind-driven resistance method, in which the surface resistance is calculated as an empirical parameter (reflecting surface collection efficiency) divided by the friction velocity (Gallagher et al., 2002).

Cloud scavenging of aerosol species is calculated following Giorgi and Chameides (1985). The fractional removal rate is equal to its in-condensate fraction multiplied by the fractional removal rate of condensate by precipitation. For hydrophilic aerosols, an empirical in-condensate fraction (ranging from 0.07 for dust to 0.3 for sulfate in large-scale clouds, and from 0.12 for dust to 0.4 for sulfate in convective clouds) is prescribed. Below-cloud aerosol washout, for large-scale precipitation only, is parameterized as described by Li et al. (2008).

Interactive simulation of aerosols from emissions in CM3 is a major change in approach from CM2.1 (Delworth et al., 2006), in which aerosol concentrations were specified. AM3 uses different emissions inventories and optical properties than AM2. AM3 also includes internal mixing and couples wet deposition to cloud microphysics. A detailed evaluation of aerosol properties is beyond the scope of this paper. Here, two fundamental CM3 aerosol properties, aerosol optical depth (AOD) and co-albedo (ratio of absorption optical depth to total optical depth), are compared with AERONET observations to show improved correlation relative to CM2.1. As analyzed in detail by Ginoux et al. (2006), the CM2.1 aerosol distribution tended to overestimate AOD in polluted regions, while underestimating biomass-burning AOD by a factor 2 or more, relative to annual-mean AOD measured by AERONET sun photometers (Holben et al., 1998) (Figs. 3a and b). Ginoux et al. (2006) also indicate that sea-salt mass was largely underestimated but compensated in marine environment by excessive sulfate scattering. The best represented environment was in dusty regions. Figs. 3c and d show a reduction in these biases, particularly in biomass burning regions, but also in polluted regions. Note that the model results are averaged from 1981 to 2000, while most AERONET sun photometers began to operate in the mid nineties or early 21st century. Since sulfur emission has decreased since the mid-nineties, simulated AOD values are likely higher than observed. Co-albedo measures aerosol absorption, and the model absorption has largely decreased from CM2.1 to CM3, agreeing much better with AERONET to generally within a factor of two at most stations (Fig. 4). This major change, which is particularly evident over regions of biomass burning, is due to several factors but primarily a decrease of black-carbon emission. The decrease in black-carbon emission, from 11 Tg $yr^{-1}$in AM2 (Horowitz, 2006) to 8.2 Tg $yr^{-1}$in AM3, is partly compensated by increased absorption due to internal mixing of sulfate and black carbon. Unlike the direct measurement of AOD by sun photometers, co-albedo is retrieved by an inversion of Almucantar data (Dubovik and King, 2000), and, to limit error of the retrieved values, only data with AOD greater than 0.45 are inverted. Thus, AERONET co-albedo is representative of heavy polluted, but not pristine, environments. Another bias to consider is that AERONET values are at 440 nm (blue), while the simulated aerosol properties are only archived at 550 nm (green). The subsequent bias will depend on the spectral variation of aerosol absorption. In biomass burning, smoke absorbs more in the green than the blue part of the solar spectrum, so the model co-albedo at 550 nm should be higher than at 440 nm. In dusty environments, the opposite should be true. These biases may partially explain the persisting discrepancies in Figs. 4c and d for CM3.

Clear-sky downward shortwave radiation in CM3 is generally larger in CM3 than CM2.1 and closer to observations from the Baseline Surface Radiation Network (BSRN, http://gewex-rfa.larc.nasa.gov) (Fig. 5). The increases in clear-sky downward shortwave radiation are due to reduced aerosol direct effects in CM3. Improved agreement of CM3 simulations of downward clear-sky surface shortwave radiation, optical depths, and co-albedo with BSRN and AERONET provides strong evidence that the direct effects of aerosols are more realistically simulated in CM3.

Aerosol activation into cloud droplets follows the parameterization detailed in Ming et al. (2006). Sulfate and sea salt aerosols are treated as pure ammonium sulfate and sodium chloride, respectively, in terms of cloud condensation nuclei efficiency, while organic aerosol is assumed to be partially soluble (Ming and Russell, 2004). Black carbon is assumed to be insoluble and externally mixed with soluble species. However, sulfate and black carbon are treated as an internal mixture for radiation calculations. The size distributions of organic and sea salt aerosols remain unchanged regardless of ambient conditions. Sulfate is assumed to be entirely in the accumulation mode if its concentration is above 0.3 $\mu$g m$^{-3}$. Otherwise, it is partitioned between the nucleation and accumulation modes depending on the abundance of primary aerosols (i.e., organics, sea salt, black carbon, and dust). The fraction of sulfate mass in the nucleation mode is 1 when the concentration of primary aerosols is less than 0.5 $\mu$g m$^{-3}$, and decreases linearly to 0 when it exceeds 1.0 $\mu$g m$^{-3}$. This choice is based upon the consideration that that gas-to-particle conversion in polluted conditions occurs mainly through condensation onto pre-existing particles, as opposed to nucleation.

Updraft velocities at cloud base and at the time of cloud formation are used to drive aerosol activation within shallow cumulus and stratiform clouds, respectively. Vertical velocities for shallow cumulus are provided directly by the Bretherton et al. (2004) shallow cumulus parameterization. The procedure for generating the probability distribution functions for updraft velocities in stratiform clouds is described in Section 3d. Due to the absence of ice nucleation and limited treatment of microphysics generally in deep convection (in which substantial vertical accelerations can occur well above cloud base, leading to activation above cloud base), aerosol activation is not treated in deep convection. The consequences of this omission are not clear, and the matter is a high priority for future research.

A major motivation for including aerosol activation in AM3 is to enable simulation of cloud droplet sizes, which in turn partially determine the radiative and macrophysical properties of clouds, i.e., aerosol indirect effects. Droplet sizes have been evaluated using a simple simulator for the Moderate Resolution Imaging Spectroradiometer (MODIS) (King et al., 2003) satellite. For every sub-grid column generated with the stochastic cloud scheme of Pincus et al. (2005) and Pincus et al. (2006), cf. Section 3a, the radii for these liquid cloud layers in the top two units of cloud optical depth are averaged to produce a MODIS-like cloud-top radius. All cloudy sub-grid columns are given equal weight in calculating the grid-mean radius.

Many general patterns from MODIS (Collection 5) are captured in AM3, including increases in droplet sizes in the oceans off the east coasts of most continents and the January-to-July decrease in droplet sizes over sub-tropical South America and Africa (Fig. 6). The amplitudes of the changes are generally smaller in AM3 than in MODIS, though.

*g. Tropospheric and Stratospheric Chemistry*

In AM3, the chemistry models of Horowitz et al. (2003) for the troposphere and Austin and Wilson (2006) for the stratosphere are merged. The chemical system is solved using a fully implicit Euler backward method with Newton-Raphson iteration, as in Horowitz et al. (2003). Merging the two models consisted mainly of augmenting the tropospheric model with species (including halogens and atomic hydrogen) and reactions, primarily gas-phase halogen reactions, stratospheric and mesospheric photolysis reactions, and heterogeneous reactions on stratospheric aerosols. Reaction rates follow recommendations from Sander et al. (2006). The oxidation of sulfur dioxide and dimethyl sulfide to form sulfate aerosol is fully coupled with the gas-phase chemistry. Clear-sky photolysis frequencies are calculated using a multivariate interpolation table derived from the Tropospheric Ultraviolet-Visible radiation model (Madronich and Flocke, 1998), with an adjustment applied for the effects of large-scale clouds, as described by Brasseur et al. (1998).

Monthly mean dry-deposition velocities for gas-phase species (except for ozone and peroxyacetyl nitrate, PAN) are from Horowitz et al. (2003) and were calculated off-line using resistance in series (Wesely, 1989; Hess et al., 2000). Deposition velocities for ozone were taken from Bey et al. (2001) and those for PAN from a MOZART-4 simulation in which it was calculated interactively to reflect the updates described by Emmons et al. (2010).

Cloud scavenging of gas-phase species is treated as for aerosols (Section

3f), except the in-condensate fraction is determined by Henry's law equilibrium. Below-cloud washout is calculated only for large-scale precipitation and is based on Henry's law, as in Brasseur et al. (1998).

Halogens are treated in a similar manner to Austin and Wilson (2006), described further in Austin and Wilson (2010). Specifically, the rates of change of inorganic chlorine and inorganic bromine are parameterized to minimize the need to transport additional tracers in the model. Also as described in Austin and Wilson (2010), heterogeneous reactions are included on ice and nitric acid trihydrate polar stratospheric clouds (PSCs) and in liquid ternary solution (LTS) aerosols. The PSCs are taken to be in thermodynamic equilibrium with the local conditions and calculated as in Hanson and Mauersberger (1988). The reaction rates in LTS are treated as in Carslaw et al. (1995). Mass accommodation coefficients and reaction probabilities are taken from Sander et al. (2006).

Compared to the Randel and Wu (2007) climatology, general features of the annual-mean, zonally averaged ozone for the period 1980-1999 are well produced with a tropical peak near 10 hPa but with much lower ozone in the middle and high latitudes (Fig. 7). The tropical concentration peak is slightly larger than observed, at just over 11 ppmv, compared with the observed 10.5 ppmv, but there is insufficient ozone in the high latitudes, which is likely related to model transport. The seasonal variation of total column ozone (Fig. 8) is very similar to Total Ozone Mapping Spectrometer (TOMS) (Stolarski and Frith, 2006) for the decades of the 1980s and 1990s. In the

1980s, before significant ozone destruction, the model shows low tropical ozone, consistent with observations throughout the year. In middle and high latitudes, the annual variation is well reproduced, but the column ozone amounts are biased low in high northern latitudes, reflecting the bias shown in Fig. 7. In the Southern Hemisphere, the peak column amounts in spring near 60$^{\mathrm{O}}$S are simulated to be larger than observed. Similar features are also present in the 1990s. The simulated ozone hole is deeper than observed and lasts longer into summer, although it is smaller in physical area. In the annual mean, the biases are generally small (Fig. 8e), under 5%, but are larger in the Southern Hemisphere and dominated by the spring period indicated above.

## 4. Basic Simulation Characteristics

### *a. Boundary conditions and integrations*

AM3 and the land model were integrated with prescribed sea-surface temperatures, sea-ice coverage, and sea-ice albedo to demonstrate their behavior with realistic boundary conditions. These integrations will be contrasted in this section with observations and with simulations in which AM3 served as the atmospheric component of CM3.

Observed sea-surface temperatures and sea ice for the uncoupled integrations are from Rayner et al. (2003). Except as noted below, the period of integration is 1980 to 2000, with averages taken from 1981 to 2000. Initial conditions for the atmospheric model are drawn from the AM3 developmental integrations.

For the coupled integrations, CM3 was spun up for several centuries with 1860 trace gas concentrations and emissions, as described in Sections 3a and 3f. Following the spin-up, time-varying trace gas concentrations and emissions were imposed over the period 1860-2005. Anthropogenic aerosols (through both direct and indirect effects) and trace gases force climate between 1860 and 2000. The CM3 global-mean temperature (for a five-member ensemble) increases by 0.32$^{\text{O}}$C from the 1881-1920 period to the 1981-2000 period. The corresponding increases in the Climate Research Unit (CRU) observations (Brohan et al., 2006), Goddard Institute for Space Studies observations (http://data.giss.nasa.gov/gistemp/tabledata/GLB.Ts+dSST.txt) and a five-member CM2.1 ensemble (Knutson et al., 2006) are 0.56$^{\text{O}}$C, 0.52$^{\text{O}}$C, and 0.66$^{\text{O}}$C, respectively. Observed warming is intermediate between the CM2.1 and CM3 warming. In the following sections, CM3 analyses are restricted to 1981-2000 averages. Considerable inter-ensemble variability is likely at higher time resolution.

### *b. Radiation and Surface Fluxes*

Annual-mean short-wave absorption by the earth-atmosphere system in AM3 and the Earth Radiation Budget Experiment (ERBE) (Harrison et al., 1990) (Fig. 9) agree within 5 W m$^{-2}$over most of North America, the central Pacific Ocean, and southern Europe. AM3 exhibits negative biases in the tropical Indian and western Pacific Oceans, where excessive cloudiness and precipitation occur. Positive biases characterize the oceans off the subtropical west coasts of Africa, South America, and North America, where marine stratus is inadequate. Problematic marine stratus persists from AM2 (GFDL GAMDT, 2004), perhaps not surprisingly, given that the parameterizations for boundary layers and cloud macrophysics have not been changed in ways expected to remedy this deficiency. The marine stratocumulus biases are slightly smaller in the CM3 integrations than the AM3 integrations, suggesting a response to a small change in SSTs. Simultaneously, negative biases in the tropical oceans, consistent with a double ITCZ, emerge in the CM3 integration. A positive bias over the Amazon, consistent with insufficient convection, is considerably more apparent in the CM3 integration than in the AM3 integration. The behavior of the corresponding fields for outgoing longwave radiation (OLR) is consistent with the short-wave changes (Fig. 10). The corresponding fields for outgoing longwave radiation (OLR) are consistent with the short-wave changes in regions of deep convection. (Fig. 10). In particular, the AM3 OLR exhibits negative biases in the tropical Indian Ocean and west Pacific, where excessive high cloudiness occurs in association with deep convection (Fig. 10c). The double ITCZ in CM3 is evident in the splitting of the negative tropical OLR bias in the Pacific Ocean, separated by a zone of positive bias (Fig. 10d). The positive OLR bias over the Amazon in CM3 results from insufficient high cloudiness and convection (Fig. 10d).

To present a statistical summary of the radiation balances in AM3 and

CM3, Taylor diagrams (Gates et al., 1999; Taylor, 2001) (Fig. 11) are constructed using ERBE observations from 1985-1989 (Harrison et al., 1990) and observations from the Clouds and the Earth's Radiant Energy System (CERES) satellites from 2000-2005. The CERES observations are analyzed in several ways: CERES-ES4-ERBE-like, CERES-SRB-GEO, CERES-SRB-nonGEO (Wielicki et al., 1996), and CERES-Energy Balanced and Filled (EBAF) (Loeb et al., 2009). (Observations available at http://eosweb.larc.nasa.gov/PRODOCS/ceres/table_ceres.html). Shortwave and net radiation have similar root-mean-square (RMS) errors and correlation relative to observations for both AM3 and CM3. ERBE and CERES observations differ by about as much as the modeled results do from the CERES results, and the various CERES analyses differ little among themselves. AM3 and CM3 OLR RMS differences from ERBE are two to three times larger than those of shortwave and net radiation. Note that the RMS differences in Fig. 11 are normalized by the standard deviation of the ERBE observations and that the ERBE shortwave standard deviation is also two to three times larger than that of the ERBE OLR. The spread among the CERES observations themselves is somewhat greater for shortwave and longwave cloud forcing (Figs. 11d and e) than for shortwave radiation and OLR, as are the differences between ERBE and CERES observations. AM3 and CM3 differ more between themselves than they did for OLR and shortwave radiation, consistent with the cloud differences between AM3 and CM3 evident in Figs. 9c, 9d, 10c, and 10d, for example, in the ITCZ and regions of marine stratus. Pincus et al. (2008)

note that cloud forcing is a more difficult field for models to simulate than total fluxes, which are to an appreciable extent controlled by the geometry of solar insolation. In that light, it is noteworthy that shortwave cloud forcing in AM3 compares more favorably with ERBE and CERES than AM2 (Fig. 11d). Correlations and root mean square differences between both atmospheric models and observations are comparable for longwave cloud forcing, but AM3 has more spatial variability than observed, while AM2 has less.

AM3 and CM3 include the Cloud Feedback Model Intercomparison Project's Observation Simulator Package (COSP, http://cfmip.metoffice.com/). Among its components, the package includes simulators for the CALIPSO satellite lidar (Chepfer et al., 2008) and CloudSat radar (Bodas-Salcedo et al., 2008) which permit comparison of model cloud fields to the vertical structure of clouds provided by these new instruments. As an example, CALIPSO observations of cloud fraction for January 2007 (Chepfer et al., 2010) and the simulated cloud fractions from AM3 show broad, qualitative agreement, while showing biases consistent with other fields sensitive to cloudiness (Fig. 12). For example, AM3 simulates smaller cloud fractions than CALIPSO observes off the west sub-tropical coasts of North America, South America, and Africa, consistent with positive ERBE shortwave biases in these regions (Figs. 9c and d).

For coupling AM3 with ocean models, the surface energy balance (including latent and sensible heat fluxes, in addition to radiative fluxes) is crucial and not related trivially to the top-of-atmosphere radiation balance. The implied ocean heat transport (OHT) is the heat transport implied in the ocean to balance surface fluxes. Although considerable uncertainty exists in diagnosing implied ocean heat transports from observations (e.g., Large and Yeager, 2009; Griffies et al., 2009), agreement between these transports in uncoupled atmospheric models and observational estimates has been found to favor successful coupling with ocean models. The AM3 implied OHT generally fall within or close to observational estimates of Ganachaud and Wunsch (2003) and Trenberth and Caron (2001), except for the Indo-Pacific Ocean south of $30^{\mathrm{O}}$S (Fig. 13).

### *c. Dynamics*

AM3's mid-latitude westerly jets in the troposphere are about 10% stronger than in the ERA-40 re-analysis (Uppala et al., 2005) (Fig. 14). A small area of weak, spurious westerlies appears in the equatorial stratosphere around 10 hPa, and stratospheric westerlies at polar latitudes can be over 50% stronger than in ERA-40. In the troposphere, westerly biases are smaller in CM3 than AM3 in the Southern Hemisphere but larger in the Northern Hemisphere.

Wind stresses in uncoupled models, along with implied OHT, are important to successful coupling. Wind stresses over the Atlantic and Pacific Oceans for AM3 and CM3 are generally within or close to the observational estimates from the Comprehensive Ocean-Atmosphere Data Sets (COADS) (da Silva et al., 1994; Woodruff et al., 1987), ECMWF re-analysis (Gibson et al., 1997), and the ERS satellite scatterometer (CERSAT-IFREMER, 2002)

(Fig. 15). The largest AM3 Pacific departures from observations are in the Southern Hemisphere, where CM3 stresses agree better with observations. The largest Atlantic departures for CM3 are in the Northern Hemisphere, where AM3 agrees better with observations.

In AM3, Northern Hemisphere December-January-February (DJF) sea-level pressures (SLP) are biased high over most of the middle latitudes with a mixed difference pattern in the Arctic, compared to the NCEP-NCAR re-analysis (Kalnay et al., 1996) (Fig. 16). CM3 differences over the Atlantic are similar in pattern to AM3 but larger in magnitude, but a negative bias characterizes the Pacific. The maximum positive bias in the Arctic is less than half as large as in AM2 (cf., Fig. 6 in GFDL GAMDT (2004)).

The magnitudes of the errors in the DJF stationary waves (time-mean departures of the 500 hPa geopotential height from its zonal mean) are noticeably larger in CM3 than AM3 (Fig. 17). The amplitudes of the waves are larger over Europe, east Asia, and northeast North America in CM3, and the waves are shifted slightly eastward over North America in CM3, relative to AM3. In the Southern Hemisphere, the magnitudes of the departures from the zonal mean are generally larger in AM3.

A measure of the AM3's skill in simulating a key aspect of the El Niño-Southern Oscillation is its modeled relationship between tropical SST and the global precipitation pattern. This pattern can be depicted as the product of the standard deviation of the Niño-3 index and regression coefficients between the Niño-3 index and precipitation. This pattern corresponds to

AM3's precipitation response to a temperature anomaly of one standard deviation in the Niño-3 region. (The Niño-3 index is the average SST anomaly over the region $5^{\circ}$S-$5^{\circ}$N, $150^{\circ}$-$90^{\circ}$W.) Although the patterns in both AM3 and CM3 appear to be more zonal than those based on the GPCP analysis (Huffman et al., 1997), broad features of the observed pattern are simulated (Fig. 18).

AM3's skill in simulating temperature and pressure patterns associated with the Northern Annular Mode (NAM), also referred to as the Arctic Oscillation, can be similarly assessed. These patterns can be be depicted as the product of the standard deviation of the NAM index and the regression coefficients between the NAM index and the field of interest. (The NAM index is the first principal component of April-November monthly SLP north of $20^{\circ}$N.) The basic structures of temperature and pressure anomalies are similar in AM3 and observations, with magnitudes of AM3 pressure anomalies somewhat smaller (larger) than observed over Greenland and Asia (North Pacific) (Fig. 19). The magnitudes of temperature anomalies in AM3 are larger than observed at high latitudes and over the Pacific.

The frequency of tropical cyclones, diagnosed using the method of Vitart et al. (1997), with observations from the U.S. National Hurricane Center (http://www.nhc.noaa.gov/pastall.shtml#hurdat) for the Atlantic and eastern north Pacific and from the U.S. Navy (http://www.usno.navy.mil/NOOC/nmfc-ph/RSS/jtwc/best_tracks) for other basins, is greater than simulated in AM3 and CM3 (Fig. 20), although many features of their distribution are captured. Total tropical cyclone frequencies are 28.2, 37.7, and 87.7 storms per year for AM3, CM3, and observations, respectively. The frequency of storms in CM3 is 1.34 times that of AM3, consistent with the sensitive dependence of the behavior of tropical cyclones on the details of SST in models with much higher resolution and greater capabilities for cyclone simulation (Zhao et al., 2009; Bender et al., 2010).

The AM3 tropical ($15^{\mathrm{O}}$S to $15^{\mathrm{O}}$N) wave spectrum has been evaluated in the format of Wheeler and Kiladis (1999). AM3 is essentially without Kelvin waves or a Madden-Julian Oscillation (MJO) in contrast to the analysis based on OLR observations (Liebmann and Smith, 1996) (Fig. 21a,c). The simulated tropical wave spectrum is very sensitive to the closure and trigger used for the deep-cumulus parameterization (Lin et al., 2006). In experimental integrations with AM3, the CAPE relaxation closure described in Section 3e was replaced by Zhang's (2002) closure and a trigger requiring time-integrated low-level lifting sufficient to move a parcel from the boundary layer to the level of free convection (cf., Eqs. (6) and (7) in Donner et al. (2001)). Zhang's (2002) closure balances changes in CAPE by convection with changes in CAPE by non-convective processes above the PBL, i.e., CAPE changes arising only from changes in the environment of a cumulus parcel. Effectively, Zhang's (2002) closure imposes a balance between the vertical integrals of large-scale advection of dry static energy and convective heating (Zhang, 2009). Use of the Zhang (2002) closure with a lifting trigger produces a stronger Kelvin wave and MJO, though both remain weaker than observed (Fig. 21b). The closure and trigger for the cumulus parameterization impact many aspects of the simulated general circulation. For example, unlike the tropical-wave spectrum, the annual-mean precipitation is more realistic in AM3 with the CAPE relaxation closure. The promising simulation of the tropical wave spectrum (and evidence in its favor from field programs, e.g., Zhang (2002) and Donner and Philips (2003)), suggest further research as to its impact on other aspects of ocean-atmosphere coupled simulations as a high priority. (These sensitivity experiments are five-year integrations using climatological 1981-2000 SSTs.)

### *d. Thermodynamics and Precipitation*

Tropospheric temperatures in AM3 and CM3 are generally within $2^{\mathrm{O}}$C of ERA-40 re-analysis (Uppala et al., 2005), with CM3 slightly cooler than AM3 (Fig. 22). Except in polar regions at pressures greater than 5 to 10 hPa, AM3 and CM3 stratospheric temperatures are generally higher than those of ERA-40.

Compared to observed SST (http://www-pcmdi.llnl.gov/projects/amip/AMIP2EXPDSN/BCS_OBS/amip2_bcs.htm), warm biases in CM3 are evident off the sub-tropical west coasts of North and South America and Africa (Fig. 23), consistent with low-cloud errors also apparent in absorbed shortwave radiation (Fig. 9c and d). Warm biases north of Antarctica are consistent with shortwave errors in CM3, which develop as a result of ocean-atmosphere coupling (Fig. 9c and d). A broad cold bias of 2 to 3 $^{\mathrm{O}}$C prevails over the middle latitudes of the west and central Pacific, and a complex error pattern of varying signs, associated with details of the Gulf Stream simulation, characterizes the North Atlantic.

Both AM3 and CM3 capture general features of CRU temperature observations (Brohan et al., 2006) at 2m over land areas (Fig. 24). Eurasia, North America, and Africa are slightly cooler in CM3 than in AM3. Excessive variability of these temperatures compared to CRU observations is reduced in CM3, relative to CM2 (Table 2).

AM3 precipitation in tropical oceans is excessive compared with GPCP v. 2 observations (Adler et al., 2003), by as much as 3 to 5 mm $d^{-1}$(Fig. 25). Relative to AM2.1, the AM3 Amazon simulation has improved markedly (cf., Fig. 17, Delworth et al., 2006), and reduced the summer dry bias in the southern Great Plains of North America. CM3 develops a double ITCZ, which is considerably less evident in AM3. A moist bias over the western United States and a dry bias over northern South America develop in CM3 but are not evident in AM3. A moist bias over southern Africa is stronger in CM3 than AM3. As for the tropical-wave spectrum (Fig. 21), the distribution of precipitation intensity depends strongly on the closure and triggers for deep convection. As an example, the CAPE-relaxation closure used in AM3 fails to capture observed high-intensity precipitation events over tropical land areas (Fig. 26). The closure balancing convective changes in CAPE against changes in CAPE due to changes in the environment of cumulus parcels, in conjunction with a low-level lift trigger, does so. (The observed distribution of precipitation intensities is from the Tropical Rainfall Measuring Mission, TRMM 3B42 (V6) (Huffman et al., 2007), http://disc.sci.gsfc.nasa.gov/precipitation). As noted in Section 4c, future research on alternatives to the CAPE-relaxation closure is planned.

## 5. Conclusion

AM3 and CM3 have been formulated to enable study of several issues in climate and climate change which could be addressed in only limited ways with earlier GFDL coupled GCMs. These issues include cloud-aerosol interactions in the climate system, tropospheric and stratospheric chemistry, and interactions between the troposphere and stratosphere which have been identified as important in decadal variability (e.g., Southern Hemisphere Annular Mode). AM3 has increased vertical resolution and extent in its stratosphere, relative to AM2.

Despite major changes in the dynamical core and parameterizations for cloud microphysics (physically based aerosol activation), cloud macrophysics (sub-grid vertical velocities, used for aerosol activation), and deep and shallow cumulus convection, overall statistics characterizing key climate fields change only slightly relative to AM2 and CM2.1 (Fig. 27). AM3 compares favorably to models in the Atmospheric Model Intercomparison Program (AMIP) at the Project for Climate Model Diagnosis and Intercomparison (PCMDI) for phase 3 of the Climate Model Intercomparison Project (CMIP3) (Meehl et al., 2007) whose coupled simulations have performed well (Reichler and Kim, 2008). Relative to AM2 and CM2.1, several notable improvements in AM3 and CM3 are not evident in Fig. 27, as discussed elsewhere: (1) AM3 has a smaller Amazon precipitation bias (important for future coupling with a carbon-cycle model) and summer dry bias in the North American southern Great Plains. (2) AM3's simulation of shortwave cloud forcing agrees better with ERBE and CERES observations than AM2's. (3) The simulation of Arctic SLP and sea ice in CM3 have improved relative to CM2.1. (4) Aerosol direct effects are more realistic in AM2, as evidenced by better agreement of clear-sky downward shortwave radiation with BSRN and optical depths and co-albedos with AERONET.

The evolution of CM3 with aerosol-cloud interactions from pre-industrial to present-day conditions produces global and regional temperature patterns that are realistic during the late 20th century (Figs. 22, 23, 24, and 27). CM3 treats both direct and indirect aerosol effects (aerosol-cloud interactions). CM2.1, which treated only direct aerosol effects, also simulated the climate of the late 20th century realistically (Knutson et al., 2006) but did so without including aerosol-cloud interactions, which produce cooling. Both CM2.1 and CM3 achieve realistic late-20th century global temperatures by offsetting anthropogenic warming by greenhouse gases with aerosol effects. In CM3, the aerosols act both directly and through cloud-aerosol interactions, while in CM2.1 aerosols acted only through direct effects. Together, the increased realism of CM3's direct aerosol effect relative to CM2.1 and the general agreement of CM3's late-20th century warming with observations suggest that CM3's treatment of aerosol indirect effects is more plausible than the absence of aerosol indirect effects in CM2.1.

AM3 simulates key observed features of the stratospheric ozone distribution and the evolution of the stratospheric ozone hole.

High-priority future development should address ongoing biases in subtropical marine stratus in both AM3 and CM3. The emergence of a double ITCZ and dry bias in the Amazon when AM3 is coupled to an ocean model is also an important deficiency. Improved simulation of the intensity of the precipitation distribution and tropical waves, especially the MJO, also deserves attention. Addressing biases in marine stratus will require changing the behavior of stratiform macrophysics, most likely by a combination of changes in vertical resolution and formulation (Guo et al., 2010). The closure for the cumulus parameterization appears to be a promising target for increased realism of higher-frequency variability and precipitation intensity. The implementation of aerosol-cloud interactions in AM3 does not include deep convective clouds or ice clouds. Emphasis should be placed on improving the physical realism of convective microphysics and ice microphysics, with double-moment microphysics offering advantages of consistent treatment of ice and liquid particles. With respect to the stratosphere, improvements in the parameterization of gravity waves are required, and the absence of a quasi-biennial oscillation is a serious deficiency requiring attention.

*Acknowledgments.* We thank Jeff Varanyak for assisting with figure preparation. Reviews of an early draft by Tom Delworth and Gabriel Lau are appreciated.

We acknowledge the modeling groups, PCMDI, and the World Climate Research Program's (WCRP's) Working Group on Coupled Modelling for their roles in making available the WCRP CMIP3 multi-model dataset. Support of this dataset is provided by the Office of Science, U.S. Department of Energy.

The contribution of Stephen A. Klein to this work was funded through the Regional and Global Climate Modeling and Atmospheric System Research Programs of the Office of Science in the U. S. Department of Energy and was performed under the auspices of the U. S. Department of Energy by Lawrence Livermore National Laboratory under Contract DE-AC52-07NA27344. Robert Pincus was supported by the Office of Science, U.S. Department of Energy, under contract DE FG02-03ER63561. Yanluan Lin was supported by the Office of Biological and Environmental Research, U.S. Department of Energy, under Project DE AI02-07ER64477.

The TRMM data were acquired as part of the activities of NASA's Science Mission Directorate and are archived and distributed by the Goddard Earth Sciences Data and Information Services Center.

We thank the AERONET principal investigators and their staffs for establishing and maintaining the AERONET sunphotometer sites used in this investigation.

Chris Milly's assistance in coupling LM3 to AM3 has been an important

contribution to this work.

APPENDIX 1

## CM3 Land, Ocean, and Sea-Ice Models

### *a. Land Model*

LM3, the land model coupled to AM3, is a new model for land water, energy, and carbon balance. In comparison to its predecessor (the Land Dynamics, or LaD, model (Milly and Shmakin, 2002)), LM3 includes a multi-layer model of snow pack above the soil; a continuous vertical representation of soil water that spans both the unsaturated and saturated zones; a frozen soil-water phase; a parameterization of water-table height, saturated-area fraction, and groundwater discharge to streams derived from standard groundwater-hydraulic assumptions and surface topographic information; finite-velocity horizontal transport of runoff via rivers to the ocean; lakes, lake ice, and lake-ice snow packs that exchange mass and energy with both the atmosphere and the rivers; and consistent, energy-conserving accounting of sensible heat content of water in all its phases. Carbon balance and the determination of vegetation structure, phenology, and function are accomplished as in the model LM3V (Shevliakova et al., 2009).

In stand-alone numerical experiments with observation-based atmospheric forcing, and in experiments coupled to AM2 and AM3, LM3 preserves the generally realistic water-balance partitioning of the LaD model; ameliorates some of the deficiencies of the LaD model previously identified; and provides qualitatively realistic estimates of physical variables that are not tracked by the LaD model.

### *b. Ocean Model*

The ocean model component of CM3 uses the MOM4p1 code (Griffies, 2009), whereas the ocean component of CM2.1 used the MOM4.0 code (Griffies et al., 2005). The physical parameterizations and grid resolution for the CM3 ocean are the same as that used in CM2.1, as detailed in Griffies et al. (2005) and Gnanadesikan et al. (2006). The single change made for CM3 concerns the numerical formulation of the vertical coordinate (Griffies et al., 2010). Tests with the new vertical coordinate in CM2.1 showed trivial climate changes to the simulation as described, for example, in Delworth et al. (2006) and Gnanadesikan et al. (2006). Hence, for purposes of the present paper, the ocean component can be considered the same as that used in CM2.1.

### *c. Sea-Ice Model*

The CM3 sea-ice is identical to that in CM2.1 (Delworth et al., 2006; Winton, 2000), except for some parameter resetting made possible by improved realism in CM3's climate in regions of sea ice. The dry snow and ice albedos in CM3 are 0.85 and 0.68, respectively. These albedos are more realistic (Perovich et al., 2002) than the corresponding values of 0.80 and 0.58 in CM2.1. The decrements to these values for melting are ramped linearly between a threshold skin temperature of $1^{\mathrm{O}}$ C below freezing in CM3 (compared to $10^{\mathrm{O}}$ C below freezing in CM2.1), and the freezing point.

Compared to observations (Hurrell et al., 2008) CM3 sea ice extent is too far south in areas of the North Atlantic east of Greenland (Fig. A1). In general, the simulation of Northern Hemisphere sea ice has improved in CM3 relative to CM2.1, but Southern Hemisphere ice concentrations remain smaller than observed (cf., Fig. 9, Griffies et al., 2010).

APPENDIX 2

## Symbols and Units

| *Symbol* | *Description* | *Units* |
|---|---|---|
| $a_k$ | constant used to calculate pressure at interface $k$ | Pa |
| $b_k$ | constant used to calculate pressure at interface $k$ | dimensionless |
| $c_0$ | lateral mixing constant for shallow cumulus | dimensionless |
| $C_A$ | vertically integrated lateral transfer of condensate from updraft cells to mesoscale updrafts | kg m$^{-2}$ s$^{-1}$ |
| $C_{mu}$ | vertically integrated condensation and deposition in mesoscale updrafts | kg m$^{-2}$ s$^{-1}$ |
| $D$ | rate of change of saturated cloud mass flux with pressure in detraining layers | s m$^{-1}$ |
| $E_{me}$ | vertically integrated condensate transfer from mesoscale updrafts to large-scale stratiform clouds | kg m$^{-2}$ s$^{-1}$ |
| $g$ | gravity constant | m s$^{-2}$ |
| $M$ | mass flux | kg m$^{-2}$ s$^{-1}$ |
| $p$ | pressure | Pa |
| $R_m$ | precipitation rate from mesoscale updrafts | kg m$^{-2}$ s$^{-1}$ |
| $X$ | mixing ratio for cloud liquid or ice; cloud fraction | kg(water) kg$^{-1}$; dimensionless |
| $z$ | height | km |
| $\gamma$ | factor relating cumulus mass flux to vertical diffusion coefficient for momentum | dimensionless |

The following apply generally:

$(\ )_{deep}$ refers to deep convective systems, comprised of cells and mesoscale circulations.

$(\ )_{meso}$ refers to mesoscale updrafts.

$(\ )_{shal}$ refers to shallow cumulus.

$(\ )_{s}$ refers to lower boundary of atmospheric model.

$(\ )^{*}$ refers to a property or process within a convective system.

$\overline{(\ )}$ refers to a large-scale average.

## REFERENCES

Adler, R.F., G.J. Huffman, A. Chang, R. Ferraro, P.-P. Xie, J. Janowiak, B. Rudolf, U. Schneider, S. Curtis, D. Bolvin, A. Gruber, J. Susskind, P. Arkin, and E. Nelkin, 2003: The version-2 global precipitation climatology project (GPCP) monthly precipitation analysis (1979-present). *J. Hydrometeorology,* **4,** 1147-1167.

Alexander, M.J., and T.J. Dunkerton, 1999: A spectral parameterization of mean-flow forcing due to breaking gravity waves. *J. Atmos. Sci.,* **56,** 4167-4182.

Alexander, M.J., and K.H. Rosenloff, 2003: Gravity-wave forcing in the stratosphere: Observational constraints from the upper atmosphere research satellite and implications for parameterization in global models, *J. Geophys. Res.,* **108,** doi:10.1029/2003JD003373.

Austin, J., and R.J. Wilson, 2006: Ensemble simulations of the decline and recovery of stratospheric ozone.*J. Geophys. Res.,***111,** D16314, doi10.1029/2005JD006907.

——, 2010: Sensitivity of polar ozone to sea surface temperatures and halogen amounts. *J. Geophys. Res.,* **115,** doi: 10.1029/2009JD013292.

Balkanski, Y., M. Schulz, T. Claquin, S. and Guibert, 2007: Reevaluation of mineral aerosol radiative forcings suggests a better agreement with satellite and AERONET data. *Atmos. Phys. Chem.,* **7,** 81-97.

Bender, M.A., T.R. Knutson, R.E. Tuleya, J.J. Sirutis, G.A. Vecchi, S.T. Garner, and I.M. Held, 2010: Modeled impact of anthropogenic warming on the frequency of intense Atlantic hurricanes. *Science,* **327,** 454-454.

Bey, I., D. J. Jacob, R. M. Yantosca, J. A. Logan, B. D. Field, A. M. Fiore, Q. Li, H. Y. Liu, L. J. Mickley, and M. G. Schultz, 2001: Global modeling of tropospheric chemistry with assimilated meteorology: Model description and evaluation. *J. Geophys. Res.,* **106,** 23,073-23,095.

Bodas-Salcedo, A., M.J. Webb, M.E. Brooks, M.A. Ringer, K.D. Williams, S.F. Milton, D.R. Wilson, 2008: Evaluating cloud systems in the Met Office global forecast model using simulated CloudSat radar reflectivities. *J. Geophys. Res.* **113,** doi:10.1029/2007JD009620.

Bower, K.N., T.W. Choularton, J. Latham, J. Nelson, M.B. Baker, and J. Jensen, 1994: A parameterization of warm clouds for use in atmospheric general circulation models. *J. Atmos. Sci.,* **51,** 2722-2732.

Brasseur, G.P., et al., 1998: MOZART, a global chemical transport model for ozone and related chemical tracers: 1. Model description. *J. Geophys. Res.,* **103,** 28,265-28,289.

Bretherton, C.S., J.R. McCaa, and H. Grenier, 2004: A new parameterization for shallow cumulus convection and its application to marine subtropical cloud-topped boundary layers. Part I: Description and 1D results. *Mon.*

*Wea. Rev.,* **132,** 864-882.

Brohan, P., J.J. Kennedy, I. Harris, S.F.B. Tett and P.D. Jones, 2006: Uncertainty estimates in regional and global observed temperature changes: a new dataset from 1850. *J. Geophys. Res.,* **111,** doi:10.1029/2005JD006548.

Carslaw, K.S., B.P. Luo, and Th. Peter, 1995: An analytic expression for the composition of aqueous $HNO_3$-$H_2SO_4$ stratospheric aerosols including gas phase removal of $HNO_3$. *Geophys. Res. Lett.*, **22,** 1877-1880.

CERSAT-IFREMER, 2002: ERS-1, ERS-2, and NSCAT. Vol. 1. Mean wind fields (MWF product). User manual. C2-MUT-W-05-IF, Brest, France. 72pp. [Available online at ftp://ftp.ifremer.fr/ifremer/cersat/documentation/gridded/mwf-ers_vol1.pdf]

Chepfer, H., S. Bony, D. Winker, M. Chiriaco, J.-L. Dufresne, and G. Séze, 2008: Use of CALIPSO lidar observations to evaluate cloudiness simulated by a climate model. *Geophys. Res. Lett.,* **35,** doi:10.1029/2008GL034207.

Chepfer, H., S. Bony, D. Winker, G. Cesana, J. L. Dufresne, P. Minnis, C. J. Stubenrauch, and S. Zeng, 2010: The GCM-Oriented CALIPSO Cloud Product (CALIPSO-GOCCP). *J. Geophys. Res.,* **115,** D00H16, doi:10.1029/2009JD012251.

Chin, M., P. Ginoux, S. Kinne, O. Torres, B.N. Holben, B.N. Duncan, R.V. Martin, J.A. Logan, A. Higurashi, T. and Nakajima, 2002: Tropospheric aerosol optical thickness from the GOCART model and comparisons with satellite and Sun photometer measurements. *J. Atmos. Sci.,* **59,** 461-483.

Cooke, W.F., C. Liousse, H. Cachier, and J. Feichter, 1999: Construction of a $1^o \times 1^o$ fossil fuel emission data set for carbonaceous aerosol and implementation and radiative impact in the ECHAM4 model. *J. Geophys. Res.,* **104,** 137-162.

da Silva, A., A.C. Young, and S. Levitus, 1994: *Algorithms and Procedures. Vol. 1, Atlas of Surface Marine Data 1994,* NOAA Atlas NESDIS 6, 83 pp.

Delworth, T.D., A.J. Broccoli, A. Rosati, R.J. Stouffer, V. Balaji, J.A. Beesley, W.F. Cooke, K.W. Dixon, J. Dunne, K.A. Dunne, J.W. Durachta, K.L.Findell, P. Ginoux, A. Gnanadesikan, C.T. Gordon, S.M. Griffies, R. Gudgel, M.J. Harrison, I.M. Held, R.S. Hemler, L.W. Horowitz, S.A. Klein, T.R. Knutson, P.J. Kushner, A.R. Langenhorst, H.-C. Lee, S.-J. Lin, J. Lu, S.L. Malyshev, V. Ramaswamy, J. Russell, M.D. Schwarzkopf, E. Shevliakova, J.J. Sirutis, M.J. Spelman, W.F. Stern, M. Winton, A.T. Wittenberg, B. Wyman, F. Zeng, and R. Zhang, 2006: GFDL's CM2 global coupled climate models-Part I: Formulation and simulation characteristics. *J. Climate,* **19,** 643-674.

Dentener, F., S. Kinne, T. Bond, O. Boucher, J. Cofala, S. Generoso, P.

Ginoux, S. Gong, J. J. Hoelzemann, A. Ito, L. Marelli, J. E. Penner, J.-P. Putaud, C. Textor, M. Schulz, G. R. van der Werf, and J. Wilson, 2006: Emissions of primary aerosol and precursor gases in the years 2000 and 1750 prescribed data-sets for AeroCom. *Atmos. Chem. Phys.,* **6,** 4321-4344.

Donner, L.J., 1993: A cumulus parameterization including mass fluxes, vertical momentum dynamics, and mesoscale effects. *J. Atmos. Sci.,* **50,** 889-906.

——, C.J. Seman, and R.S. Hemler, 2001: A cumulus parameterization including mass fluxes, convective vertical velocities, and mesoscale effects: Thermodynamic and hydrological aspects in a general circulation model. *J. Climate,* **14,** 3444-3463.

Donner, L.J., C.J. Seman, B.J. Soden, R.S. Hemler, J.C. Warren, J. Ström, and K.-N. Liou, 1997: Large-scale ice clouds in the GFDL SKYHI general circulation model. *J. Geophys. Res.,* **102,** 21,745-21,768.

Donner, L.J., and V.T. Phillips, 2003: Boundary-layer control on convective available potential energy: Implications for cumulus parameterization. *J. Geophys. Res.,* **108,** doi:10.1029/2003JD003773.

Dubovik, O. and King, M.D., 2000: A flexible inversion algorithm for retrieval of aerosol optical properties from Sun and sky radiance measurements. *J. Geophys. Res.,* **105,** doi:10.1029/2000JD900282.

Emmons, L.K., et al., 2010: Description and evaluation of the Model for Ozone and Related chemical Tracers, version 4 (MOZART-4). *Geosci. Model Dev.,* **3,** 43-67.

Freidenreich, S.M., and V. Ramaswamy, 1999: A new multiple-band solar radiative parameterization for general circulation models. *J. Geophys. Res.,* **104,** 31,389-31,409.

Fu, Q., 1996: An accurate parameterization of the the solar radiative properties of cirrus clouds for climate models. *J. Climate,* **9,** 2058-2082.

——, and K.N. Liou, 1993: Parameterization of the radiative properties of cirrus clouds. *J. Atmos. Sci.,* **50,** 2008-2025.

Fu, Q., P. Yang, and W.B. Sun, 1998: An accurate parameterization of the infrared radiative properties of cirrus clouds for climate models. *J. Climate,* **11,** 2223-2237.

Gallagher, M.W., et al., 2002: Measurements and parameterizations of small aerosol deposition velocities to grassland, arable crops, and forest: Influence of surface roughness length on deposition. *J. Geophys. Res.,* **107,** doi:10.1029/2001JD000817.

Ganachaud, A., and C. Wunsch, 2003: Large-scale ocean heat and freshwater transports during the World Ocean Circulation Experiment. *J. Climate,* **16,** 696-705.

Gates, W.L., and Co-Authors, 1999: An overview of the results of the Atmospheric Model Inter-Comparison Project (AMIP I). *Bull. Amer. Meteor. Soc.,* **80,** 29-55.

Geophysical Fluid Dynamics Laboratory Global Atmosphere Model Development Team, 2004: The new GFDL global atmosphere and land model AM2-LM2: Evaluation with prescribed SST simulations. *J. Climate,* **17,** 4641-4673.

Ghan, S.J., L. R. Leung, R.C. Easter, and H. Abdul-Razzak, 1997: Prediction of cloud droplet number in a general circulation model. *J. Geophys. Res.,* **102,** 21,777-21,794.

Gibson, J.K., P. Kallberg, S. Uppala, A. Hernandez, A. Nomura, and E. Serrano, 1997: ERA Description. Vol 1. ECMWF Re-analysis Project Rep. Series, European Centre for Medium-Range Weather Forecasts, Reading, United Kingdom, 66 pp.

Ginoux, P., M. Chin, I. Tegen, J. M. Prospero, B. Holben, O. Dubovik, and S. Lin, 2001: Sources and distributions of dust aerosols simulated with the GOCART model. *J. Geophys. Res.,* **106,** 22055-22074.

Ginoux, P., Horowitz, L.W., Ramaswamy, V., Geogdzhayev, I.V., Holben, B.N., Stenchikov, G. and Tie, X., 2006: Evaluation of aerosol distribution and optical depth in the Geophysical Fluid Dynamics Laboratory coupled model CM2.1 for present climate. *J. Geophys. Res.,* **111,** doi:10.1029/2005JD006707.

Giorgetta, M.A., E. Manzini, R. Roeckner, M, Esch, and L. Bengtsson, 2006: Climatology and forcing of the quasi-biennial oscillation in the MAECHAM5 model. *J. Climate,* **19,** 3882-3901.

Giorgi, F., and W.L. Chameides, 1985: The rainout parameterization in a photochemical model. *J. Geophys. Res.,***90,** 7872-7880.

Gnanadesikan, A., Dixon, K. W., Griffies, S. M., Balaji, V., Beesley, J. A., Cooke, W. F., Delworth, T. L., Gerdes, R., Harrison, M. J., Held, I. M., Hurlin, W. J., Lee, H.-C., Liang, Z., Nong, G., Pacanowski, R. C., Rosati, A., Russell, J., Samuels, B. L., Song, S. M., , Spelman, M. J., Stouer, R. J., Sweeney, C. O., Vecchi, G., Winton, M., Wittenberg, A. T., Zeng, F., Zhang, R., 2006: GFDL's CM2 global coupled climate models-Part 2: The baseline ocean simulation. *J. Climate,* **19,** 675-697.

Golaz, J.-C., M. Salzmann, L.J. Donner, L.W. Horowitz, Y. Ming, and M. Zhao, 2010: Sensitvity of the aerosol indirect effect to subgrid variability in the cloud parameterization of the GFDL atmosphere general circulation model AM3. *J. Climate,* submitted.

Griffies, S. M., 2009: Elements of MOM4p1. Available at http://www.gfdl.noaa.gov/fms.

——, A. Gnanadesikan, K.W. Dixon, J.P. Dunne, R. Gerdes, M.J. Harrison, A. Rosati, J. Russell, B.L. Samuels, M.J. Spelman, M. Winton, and R. Zhang, 2005: Formulation of an ocean model for global climate simulations. *Ocean Science,* **1,** 45-79.

Griffies, S.M. J. Harrison, R. C. Pacanowski, and A. Rosati, 2004: A Technical Guide to MOM4. Available at http://www.gfdl.noaa.gov/fms.

Griffies, S.M., A. Biastoch, C. Boening, F. Bryan, E. Chassignet, M. England, R. Gerdes, H. Haak, R.W. Hallberg, W. Hazeleger, J. Jungclaus, W.G. Large, G. Madec, B.L. Samuels, M. Scheinert, A. Sen Gupta, C.A. Severijns, H.L. Simmons, A.-M. Treguier, M. Winton, S. Yeager, J. Yin, 2009: Coordinated Ocean-ice Reference Experiments (COREs). *Ocean Modeling,* **26,** i-46

Griffies, S.M., M. Winton, L.J. Donner, S.M. Downes, R. Farneti, A. Gnanadesekin, L.W Horowitz, W.J. Hurlin, H.-C. Lee, J. B. Palter, B.L. Samuels, A.T. Wittenberg, B.L. Wyman, J. Yin, 2010: GFDL's CM3 coupled climate model: Characteristics of the ocean and sea ice simulations. *J. Climate,* submitted.

Guo, H., J.-C. Golaz, L.J. Donner, V.E. Larson, D.P. Schanen, and B.M. Griffin, 2010: A dynamic probability density function treatment of cloud mass and number concentrations for low level clouds in GFDL SCM/GCM. *Geosci. Model Dev. Discuss.,* **3,** 541-588.

Hanson, D.R. and K. Mauersberger, 1988: Laboratory studies of nitric acid trihydrate: Implications for the south polar stratosphere. *Geophys. Res. Lett.*, **15,** 855-858.

Harrison, E.F., P. Minnis, B.R. Barkstrom, V. Ramanathan, R.D. Cess, and G.G. Gibson, 1990: Seasonal variation of cloud radiative forcing derived from the Earth Radiation Budget Experiment. *J. Geophys. Res.,* **95,** 18,687-18,703.

Haywood, J.M. and Ramaswamy, V., 1998: Global sensitivity studies of the direct radiative forcing due to anthropogenic sulfate and black carbon aerosols. *J. Geophys. Res.,* **103,** 6043-6058.

Held, I.M., R.S. Hemler, and V. Ramaswamy, 1993: Radiative-convective equilibrium with explicit two-dimensional moist convection. *J. Atmos. Sci.,* **50,** 3909-3927.

Hess, M., P. Koepke, and I. Schult, 1998: Optical properties of aerosols and clouds: The software package OPAC. *Bull. Amer. Meteor. Soc.,* **79,** 831-844.

Hess, P.G., S. Flocke, J.-F. Lamarque, M.C. Barth, and S. Madronich, 2000: Episodic modeling of the chemical structure of the troposphere as revealed during the spring MLOPEX 2 intensive. *J. Geophys. Res.,* **105,** doi:10.1029/2000JD900253.

Heymsfield, A.J., and L.J. Donner, 1990: A scheme for parameterizing ice-cloud water content in general circulation models. *J. Atmos. Sci.,* **47,** 1865-1877.

Holben, B.N., T.F. Eck, I. Slutsker, D. Tanre, J.P. Buis, A. Setzer, E. Vermote, J.A. Reagan, Y.J. Kaufman, T. Nakajima, et al., 1998: AERONET–A federated instrument network and data archive for aerosol characterization. *Remote Sensing of Environment,* **66,** 1-16.

Holtslag, A. A. M., and B.A. Boville, 1993: Local versus nonlocal boundary-layer diffusion in a global climate model. *J. Climate,* **6,** 1825-1842.

Horowitz, L.W., 2006: Past, present, and future concentrations of tropospheric ozone and aerosols: Methodology, ozone evaluation, and sensitivity to aerosol wet removal. *J. Geophys. Res.,* **111,** doi:10.1029/2005JD006937.

Horowitz, L.W., S. Walters, D. Mauzerall, L.K. Emmons. P.J. Rasch, C. Granier, X. Tie, J.-F. Lamarque, M.G. Schultz, G.S. Tyndall, J.J. Orlando, and G.P. Brasseur, 2003: A global simulation of tropospheric ozone and related tracers: description and evaluation of MOZART, version 2. *J. Geophys. Res.,* **108,** D24, doi.10.1029/2002JD002853.

Huffman, G.J., R.F. Adler, P.A. Arkin, A. Chang, R. Ferraro, A. Gruber, J.

Janowiak, R.J. Joyce, A. McNab, B. Rudolf, U. Schneider, and P. Xie, 1997: The global precipitation climatology project (GPCP) combined precipitation data set. *Bull. Amer. Meteor. Soc.,* **78,** 5-20.

Huffman, G.J., D.T. Bolvin, E.J. Nelkin, D.B. Wolff, R.F. Adler, G. Gu, Y. Hong, K.P. Bowman, and E.F. Stocker, 2007: The TRMM multisatellite precipitation analysis (TPMA): Quasi-global, multiyear, combined-sensor precipitation estimates at fine scales. *J. Hyrodmeteor.,* **8,** 38-55.

Hurrell, J., J. Hack, D. Shea, J. Caron, and J. Rosinski, 2008: A new sea surface temperature and sea ice boundary data set for the Community Atmosphere Model. *J. Climate,* **21,** 2428-2446.

Kalnay, E., and Co-authors, 1996: The NCEP/NCAR 40-year re-analysis project. *Bull. Amer. Meteor. Soc.,* **77,** 437-471.

King, M. D.,W. P. Menzel, Y. J. Kaufman, D. Tanre, B.-C. Gao, S. Platnick, S. A. Ackerman, L. A. Remer, R. Pincus, and P. A. Hubanks, 2003: Cloud and aerosol properties, precipitable water, and profiles of temperature and humidity. *IEEE Trans. Geosci. Remote Sens.,* **41,** 442-458, doi:10.1109/TGRS.2002.808226.

Knutson, T.R., T.L. Delworth, K.W. Dixon, I.M. Held, J. Lu, V. Ramaswamy, M.D. Schwarzkopf, G. Stenchikov, and R.J. Stouffer, 2006: Assessment of twentieth-century regional surface trends using the GFDL CM2 coupled models. *J. Climate,* **19,** 1624-1651.

Kopp, G., Lawrence, G., and Rottman, G., 2005: The Total Irradiance Monitor (TIM): Science Results. *Solar Physics,* **230,** 129-140.

Lamarque, J.-F., T.C. Bond, V. Eyring, C. Granier, A. Heil, Z. Klimont, D. Lee, C. Liousee, A. Mieville, B. Owen, M.G. Schultz, D. Shindell, S.J. Smith, E. Stehfest, J. Van Aardenne, O.R. Cooper, M. Kainuma, N. Mahowald, J.R. McConnell, V. Naik, K. Riahi, and D.P. van Vuuren, 2010: Historical (1850-2000) gridded anthropogenic and biomass burning emissions of reactive gases and aerosols: Methodology and application. *Atmos. Chem. Phys. Discuss.,* **10,** 4963-5019.

Large, W.G., and S.G. Yeager, 2009: The global climatology of an interannually varying air-sea flux data set. *Clim. Dyn.,* **33,** 341-364.

Leary, C.A., and R.A. Houze, Jr., 1980: The contribution of mesoscale motions to the mass and heat fluxes of an intense tropical convective system. *J. Atmos. Sci.,* **37,** 784-796.

Li, F., P. Ginoux, and V. Ramaswamy, 2008: Distribution, transport, and deposition of mineral dust in the Southern Ocean and Antarctica: Contribution of major sources. *J. Geophys. Res.,* **113,** doi:10.1029/2007JD009190.

Liao, H. and J.H. Seinfeld, 2005: Global impacts of gas-phase chemistry-aerosol interactions on direct radiative forcing by anthropogenic aerosols and ozone. *J. Geophys. Res.*, **110**, doi:10.1029/2005JD005.

Liebmann, B., and C. A. Smith, 1996: Description of a complete (interpolated) outgoing longwave radiation dataset. *Bull. Amer. Meteor. Soc.,* **77,** 1275-1277.

Lin, J.-L., G.N. Kiladis, B.E. Mapes, K.M. Weickmann, K.R. Sperber, W. Lin, M. Wheeler, S.D. Schubert, A. Del Genio, L.J. Donner, S. Emori, J.-F. Gueremy, F. Hourdin, P.J. Rasch, E. Roeckner, and J.F. Scinocca, 2006: Tropical intraseasonal variability in 14 IPCC AR4 climate models. Part I. Convective signals. *J. Climate,* **19,** 2665-2690.

Lin, S.-J., 1997: A finite-volume integration method for computing pressure-gradient force in general vertical coordinates. *Quart. J. Roy. Meteor. Soc.,* **123,** 1749-1762.

——, 2004: A “vertically Lagrangian” finite-volume dynamical core for global models. *Mon. Wea. Rev.,* **132,** 2293-2307.

——, and R. B. Rood, 1996: Multidimensional flux-form semi-lagrangian transport schemes. *Mon. Wea. Rev.* **124,** 2046-2070.

——, 1997: An explicit flux-form semi-Lagrangian shallow water model on the sphere. *Quart. J. Roy. Meteor. Soc.,* **123,** 2477-2498.

Lock, A.P., A.R. Brown, M.R. Bush, M. Martin, and R.N.B. Smith, 2000:

A new boundary layer mixing scheme. Part I: Scheme description and single-column model tests. *Mon. Wea. Rev.,* **128,** 3187-3199.

Loeb, N., B.A. Wielicki, D.R. Doelling, G.L. Smith, D.F. Keyes, S. Kato, N. Manalo-Smith, and T. Wong, 2009: Toward optimal closure of the earth's top-of-atmosphere radiation budget. *J. Climate,* **22,** 748-766.

Louis, J.-F., 1979: A parametric model of vertical eddy fluxes in the atmosphere. *Bound.-Layer Meteor.,* **17,** 187-202.

Madronich, S. and S. Flocke, 1998: The role of solar radiation in atmospheric chemistry. *Handbook of Environmental Chemistry,* P. Boule, ed., Springer-Verlag, Heidelberg, pp. 1-26.

Manabe, S., J. Smagorinsky, and R.F. Strickler, 1965: Simulated climatology of a general circulation model with hydrologic cycle. *Mon. Wea. Rev.,* **93,** 769-798.

McFarquhar, G.M., A.J. Heymsfield, A. Macke, J. Iaquinta, and S.M. Aulenbach, 1999: Use of observed ice crystal sizes and shapes to calculate mean scattering properties and multi-spectral radiances: CEPEX April 4, 1993 case study. *J. Geophys. Res.,* **104**(D24), 31,763-31,780.

Meehl, G. A., C. Covey, T. Delworth, M. Latif, B. McAvaney, J. F. B. Mitchell, R. J. Stouffer, and K. E. Taylor, 2007: The WCRP CMIP3 multi-model dataset: A new era in climate change research.*Bull. Amer.*

*Meteor. Soc.* **88,** 1383-1394.

Milly, P.C.D., and A.B. Shmakin, 2002: Global modeling of land water and energy balances. Part I: The land dynamics (LaD) model. *J. Hydrometeorology,* **3,** 283-299.

Ming, Y., and L.M. Russell, 2004: Organic aerosol effects on fog droplet spectra. *J. Geophys. Res.*, **109**, doi:10.1029/2003JD004.

Ming, Y., V. Ramaswamy, L.J. Donner, and V.T.J. Phillips, 2006: A robust parameterization of cloud droplet activation. *J. Atmos. Sci.,* **63,** 1348-1356.

Ming, Y., V. Ramaswamy, P.A. Ginoux, and L.W. Horowitz, 2005: Direct radiative forcing of anthropogenic organic aerosols. *J. Geophys. Res.*, **110**, doi:10.1029/2004JD005.

Monahan, E. C., D. E. Spiel, and K. L. Davidsona, 1986: A model of marine aerosol generation via whitecaps and wave disruption. *Oceanic Whitecaps,* E. C. Monahan and G. Mac Niocaill, Eds., D. Reidel, 167-174.

O'Dowd, C.D.,B. Langmann, S. Varghese, C. Scannell, D. Ceburnis, and M.C. Facchini, 2008: A combined organic-inorganic sea-spray source function. *Geophys. Res. Lett.,* **35,** doi:10.1029/2007GL030331.

Perovich, D., T. C. Grenfell, B. Light, and P. V. Hobbs, 2002: Seasonal evolution of the albedo of multi-year arctic sea ice. *J. Geophys. Res.,* **107,** doi:10.1029/2000JC000438.

Pincus, R., H. W. Barker, and J. Morcrette, 2003: A fast, flexible, approximate technique for computing radiative transfer in inhomogeneous cloud fields. *J. Geophys. Res.,* **108(D13),** 4376, doi:10.1029/2002JD003322.

Pincus, R., C. P. Batstone, R. J. P. Hofmann, K. E. Taylor, and P. J. Glecker, 2008: Evaluating the present-day simulation of clouds, precipitation, and radiation in climate models. *J. Geophys. Res.,* **113,** doi:10.1029/2007JD009334.

Pincus, R., C. Hannay, S. A. Klein, K.-M. Xu, and R. Hemler, 2005: Overlap assumptions for assumed probability distribution function cloud schemes in large-scale models. *J. Geophys. Res.,* **110,** D15S09, doi:10.1029/2004JD005100.

Pincus, R., R. Hemler, and S.A. Klein, 2006: Using stochastically generated sub-columns to represent cloud structure in a large-scale model.*Mon. Wea. Rev.*, **134,** 3644-3656. doi:10.1175/MWR3257.1.

Putman, W. M. and S.-J. Lin, 2007: Finite-volume transport on various cubed-sphere grid. *J. Comput. Phys.*, **227**, 5578.

Randel, W.J. and F. Wu, 2007: A stratospheric ozone profile data set for 1979-2005: Variability, trends, and comparisons with column ozone data. *J. Geophys. Res.,* **112,** doi:10.1029/2006JD007339.

Rayner, N.A.,D.E. Parker, E.B. Horton, C.K. Folland, L.V. Alexander, and D.P. Rowell, 2003: Global analyses of sea surface temperature, sea ice, and night marine air temperature since the late nineteenth century. *J. Geophys. Res.,* **108,** doi:10.1029/2002JD002670.

Reichler, T., and J. Kim, 2008: How well do coupled models simulate today's climate? *Bull. Amer. Meteor. Soc.,* **89,** 303-311.

Rotstayn, L.D., 1997: A physically based scheme for the treatment of stratiform clouds and precipitation in large-scale models. I: Description and evaluation of microphysical processes. *Quart. J. Roy. Meteor. Soc.,* **123,** 1227-1282.

——, B.F. Ryan, and J. Katzfey, 2000: A scheme for calculation of the liquid fraction in mixed-phase clouds in large-scale models. *Mon. Wea. Rev.,* **128,** 1070-1088.

Sadourny, R. 1972: Conservative finite-difference approximations of the primitive equations on quasi-uniform spherical grids. *Mon. Wea. Rev.,* **144,** 136-144.

Sander, S.P., R.R. Friedl, D.M. Golden, M.J. Kurylo, R.E. Huie, V.L. Orkin, G.K. Moortgat, A.R. Ravishankara, C.E. Kolb, M.J. Molina, B.J. Finlayson-Pitts, 2006: Chemical kinetics and photochemical data for use in atmospheric studies. Evaluation No. 15, JPL Publication 06-2, Jet Propulsion

Laboratory, Pasadena, CA, USA.

Schwarzkopf, M.D., and V. Ramaswamy, 1999: Radiative effects of CH4, N2O, halocarbons and the foreign-broadened H2O continuum: A GCM experiment. *J. Geophys. Res.,* **104,** 9467-9488.

Shevliakova, E., S.W. Pacala, S. Malyshev, G.C. Hurtt, P.C.D. Milly, J.D. Caspersen, L.T. Sentman, J.P. Fisk, C. Wirth, C. Crevoisier, 2009: Carbon cycling under 300 years of land use change: Importance of the secondary vegetation sink.*Global Biogeochemical Cycles,* **23,** GB2022, doi:10.1029/2007GB003176.

Simmons, A.J., and D.M. Burridge, 1981: An energy and angular-momentum conserving vertical finite-difference scheme and hybrid vertical coordinates. *Mon. Wea. Rev.,* **109,** 758-766.

Slingo, A., 1989: A GCM parameterization for the shortwave radiative properties of water clouds. *J. Atmos. Sci.,* **46,** 1419-1427.

Stenchikov, G., K. Hamilton, R. J. Stouffer, A. Robock, V. Ramaswamy, B. Santer, and H.-F. Graf, 2006: Arctic Oscillation response to volcanic eruptions in the IPCC AR4 climate models. *J. Geophys. Res.,* **111,** D07107, doi:10.1029/2005JD006286.

Stern, W.F., and R.T. Pierrehumbert, 1988: The impact of an orographic gravity wave drag parameterization on extended-range predictions with a GCM. *Preprints, Eighth Conf. on Numerical Weather Prediction,* Baltimore, MD, Amer. Meteor. Soc., 745-750.

Stolarski, R. S., and S. Frith, 2006: Search for evidence of trend slowdown in the long-term TOMS/SBUV total ozone data record: The importance of instrument drift uncertainty. *Atmos. Chem. Phys.,* **12,** 4057-4065.

Tang, I.N., and H.R. Munkelwitz, 1994: Water activities, densities, and refractive indices of aqueous sulfates an sodium nitrate droplets of atmospheric importance. *J. Geophys. Res.,* **99,**18801-18808.

Tang, I. N., A. C. Tridico, and K. H. Fung, 1997: Thermodynamic and optical properties of sea-salt aerosols. *J. Geophys. Res.,* **102,** 23269-23276.

Taylor, K.E., 2001: Summarizing multiple aspects of model performance in a single diagram. *J. Geophys. Res.,* **106,** 7183-7192.

Thompson, D.W.J., and S. Solomon, 2006: Interpretation of recent Southern Hemisphere climate change. *Science,* **296,** 895-899.

Tie, X., S. Madronich, S. Walters, D. P. Edwards, P. Ginoux, N. Mahowald, R. Zhang, C. Lou, and G. Brasseur, 2005: Assessment of the global impact of aerosols on tropospheric oxidants. *J. Geophys. Res.,* **110,** doi:10.1029/2004JD005359.

Tiedtke, M., 1993: Representation of clouds in large-scale models. *Mon.*

*Wea. Rev.,* **121,** 3030-3061.

Trenberth, K.E., and J.M. Caron, 2001: Estimates of meridional atmosphere and ocean heat transports. *J. Climate,* **14,** 3433-3443.

Uppala, S.M., Kålberg, P.W., Simmons, A.J., Andrae, U., da Costa Bechtold, V., Fiorino, M., Gibson, J.K., Haseler, J., Hernandez, A., Kelly, G.A., Li, X., Onogi, K., Saarinen, S., Sokka, N., Allan, R.P., Andersson, E., Arpe, K., Balmaseda, M.A., Beljaars, A.C.M., van de Berg, L., Bidlot, J., Bormann, N., Caires, S., Chevallier, F., Dethof, A., Dragosavac, M., Fisher, M., Fuentes, M., Hagemann, S., Hólm, E., Hoskins, B.J., Isaksen, L., Janssen, P.A.E.M., Jenne, R., McNally, A.P., Mahfouf, J.-F., Morcrette, J.-J., Rayner, N.A., Saunders, R.W., Simon, P., Sterl, A., Trenberth, K.E., Untch, A., Vasiljevic, D., Viterbo, P., and Woollen, J. 2005: The ERA-40 re-analysis. *Quart. J. R. Meteorol. Soc.,* **131,** 2961-3012, doi:10.1256/qj.04.176.

Vitart, F., J.L. Anderson, and W.F. Stern, 1997: Simulation of interannual variability of tropical storm frequency in an ensemble of of GCM integrations. *Mon. Wea. Rev.,* **129,** 2521-2537.

Wesely, M.L., 1989: Parameterization of surface resistance to gaseous dry deposition in regional-scale numerical models. *Atmos. Environ.,* **23,** 1293-1304.

Wheeler, M., and G.N. Kiladis, 1999: Convectively coupled equatorial waves. Analysis of clouds and temperature in the wavenumber-frequency domain. *J. Atmos. Sci.,* **56,** 374-399.

Wielicki, B.A., B.R. Barkstrom, E.F. Harrison, R.B. Lee III, G.L. Smith, and J.E. Cooper, 1996: Clouds and the Earth's Radiant Energy System (CERES): An earth observing system experiment. *Bull. Amer. Meteor. Soc.,* **77,** 853-868.

Wilcox, E.M., and L.J. Donner, 2007: The frequency of extreme rain events in satellite rain-rate estimates and an atmospheric general circulation model. *J. Climate,* **20,** 53-69.

Winton, M., 2000: A reformulated three-layer sea ice model. *J. Atmos. Ocean. Technol.,* **17,** 525-531.

Woodruff, S.D.,R.J. Slutz, R.L. Jenne, and P.M. Steurer, 1987: A Comprehensive Ocean-Atmosphere Dataset. *Bull. Amer. Meteor. Soc.,* **68,** 1239.

Zhang, G., 2002: Convective quasi-equilibrium in mid-latitude continental environment and its effect on convective parameterization. *J. Geophys. Res.,* **107,** doi: 10.1029/2001JD001005.

——, 2009: Effects on entrainment on convective available potential energy and closure assumptions in convection parameterization. *J. Geophys.*

*Res.,* **114,** doi:10.1029/2008JD10976.

Zhang, X., W. Lin, and M. Zhang, 2007: Toward understanding the double Inter-tropical Convergence Zone pathology in coupled ocean-atmosphere general circulation models. *J. Geophys. Res.,* **112,** doi:10.1029/2006JD007878.

Zhao, M., I.M. Held, S-J. Lin, and G.A. Vecchi, 2009: Simulations of global hurricane climatology, interannual variability, and response to global warming using a 50km resolution GCM. *J. Climate,* **22,** 6653-6678.

## FIGURE LEGENDS

Fig. 1. AM3 annual-mean, zonally averaged cumulus mass fluxes for (a) all convection (except MAA), (b) cell updrafts, (c) mesoscale updrafts, (d) mesoscale downdrafts, and (e) shallow cumulus.

Fig. 2. Annual-mean, zonally averaged precipitation for (a) AM3 and (b) CM3.

Fig. 3. Climatological aerosol optical depths (550nm) from AERONET and (a), (b) CM2.1 and (c), (d) CM3. Dashed lines in (a) and (c) denote slopes of 0.5 and 2.

Fig. 4. Climatological aerosol co-albedos from AERONET (440nm) and (a), (b) CM2.1 and (c), (d) CM3 (550nm). Dashed lines in (a) and (c) denote slopes of 0.5 and 2.

Fig. 5. Surface clear-sky downward shortwave fluxes from BSRN and (a) CM2.1 and (c) CM3. Differences in these fluxes: (b) CM2.1 minus BSRN and (d) CM3 minus BSRN.

Fig. 6. Cloud-drop radius from MODIS simulator in AM3 for (a) January and (b) July. Cloud-drop radius from MODIS for (c) January and (d) July.

Fig. 7. Annual-mean, zonally averaged ozone from (a) AM3 and (b) TOMS.

Fig. 8. Vertically integrated, zonally averaged ozone for 1980-1989 from (a) TOMS, (b) AM3 and for 1990-1999 from (c) TOMS, (d) AM3. (e) Annual-mean difference between AM3 and TOMS vertically integrated, zonally averaged ozone.

Fig. 9. Annual-mean shortwave absorbed radiation for (a) AM3, (b) ERBE, (c) AM3 minus ERBE, and (d) CM3 minus ERBE.

Fig. 10. Annual-mean outgoing longwave radiation for (a) AM3, (b) ERBE, (c) AM3 minus ERBE, and (d) CM3 minus ERBE.

Fig. 11. Taylor diagrams for top-of-atmosphere (TOA) radiation balance. The root-mean-square (RMS) errors, correlations, and standard deviations are based on global, annual means.

Fig. 12. January 2007 cloud fractions from (a) AM3 CALIPSO simulator and (b) CALIPSO.

Fig. 13. Implied ocean heat transport for (a) total ocean, (b) Atlantic Ocean, and (c) Indo-Pacific Ocean. Dashed lines and vertical bars indicate range of one standard error above and below Trenberth and Caron (2001) and Ganachaud and Wunsch (2003) estimates, respectively.

Fig. 14. Annual-mean, zonally averaged zonal wind for (a) AM3, (b) ERA-40, (c) AM3 minus ERA-40, and (d) CM3 minus ERA-40.

Fig. 15. Annual-mean wind stress for (a) Pacific Ocean and (b) Atlantic Ocean.

Fig. 16. Northern Hemisphere DJF sea-level pressure minus 1013.25 hPa for (a) AM3, (b) NCEP re-analysis, (c) AM3 minus NCEP re-analysis, and (d) CM3 minus NCEP re-analysis. Contour intervals: (a), (b) 3 hPa; (c), (d) 1 hPa. Areas with mean surface pressures less than 950 hPa are masked.

Fig. 17. DJF departure from zonally averaged 500-hPa geopotential height for (a) AM3, (b) NCEP re-analysis, (c) AM3 minus NCEP re-analysis, and (d) CM3 minus NCEP re-analysis.

Fig. 18. DJF product of the standard deviation of the Niño-3 index and regression coefficient between precipitation and Niño-3 index for (a) AM3, (b) CM3, and (c) GPCP.

Fig. 19. Product of the standard deviation of the NAM index and regression coefficients between the NAM index and SLP (contours, hPa) and 2-m temperature (shading, $^{O}$C) for (a) AM3 and (b) NCEP re-analysis.

Fig. 20. Tropical-cyclone frequency for (a) AM3, (b) CM3, (c) U.S. National Hurricane Center and Navy observations.

Fig. 21. Normalized tropical symmetric OLR wavenumber-frequency power spectrum for (a) AM3, (b) AM3 with CAPE relaxation closure for deep

cumulus replaced by a closure in which CAPE tendencies in the environment of cumulus parcels are balanced by deep convection with low-level-lift trigger, and (c) OLR observations. Contour interval is .1 (shown for values 1.0 and greater) with colored shading of regions greater than 1.2 indicating power associated with MJO, Kelvin and other tropical convective waves that are significantly above an approximately red-noise background power spectra. The colored lines represent various equatorial wave dispersion curves labeled for five different equivalent depths, i.e., 8, 12, 25, 50 and 90m.

Fig. 22. Annual-mean, zonally averaged temperature for (a) AM3, (b) ERA-40 re-analysis, (c) AM3 minus ERA-40, and (d) CM3 minus ERA-40.

Fig. 23. Sea-surface temperatures for (a) CM3, (b) observations compiled at Lawrence Livermore National Laboratory (http://www-pcmdi.llnl.gov/projects/amip/AMIP2EXPDSN/BCS_OBS/amip2_bcs.htm), and (c) difference.

Fig. 24. 2-m temperatures for (a) AM3, (b) CRU, (c) AM3 minus CRU, and (d) CM3 minus CRU.

Fig. 25. Annual-mean precipitation for (a) AM3, (b) GPCP v. 2, (c) AM3 minus GPCP v. 2, and (d) CM3 minus GPCP v. 2.

Fig. 26. Precipitation intensity distribution from TRMM, AM3, and AM3 with CAPE relaxation closure for deep cumulus replaced by a closure

in which CAPE tendencies in the environment of cumulus parcels are balanced by deep convection with low-level-lift trigger.

Fig. 27. Taylor diagrams for sea-level pressure, surface temperature, precipitation, zonal surface wind stress, 200 hPa deviation of geopotential height from zonal mean, and 200 hPa zonal wind. Regions and periods for averages as indicated. The ECHAM5-MPI, UKMO_HadGEM1, and NCAR-CCSM3 results are their latest AMIP submissions to the World Climate Research Program's CMIP3. Observations of sea-level pressure, geopotential height, and winds from NCEP re-analysis; precipitation from GPCP v. 2; surface temperature from CRU; and wind stress from ERA-40.

Fig. A1. Annual-mean sea-ice extent for (a) CM3, (b) observations, and (c) difference. Sea-ice extent is defined to be 1 if sea-ice concentration is 15% or greater and 0 otherwise. Observed ice extent is computed from monthly ice concentrations following Hurrell et al. (2008). Values between 0 and 1 result from time averaging.

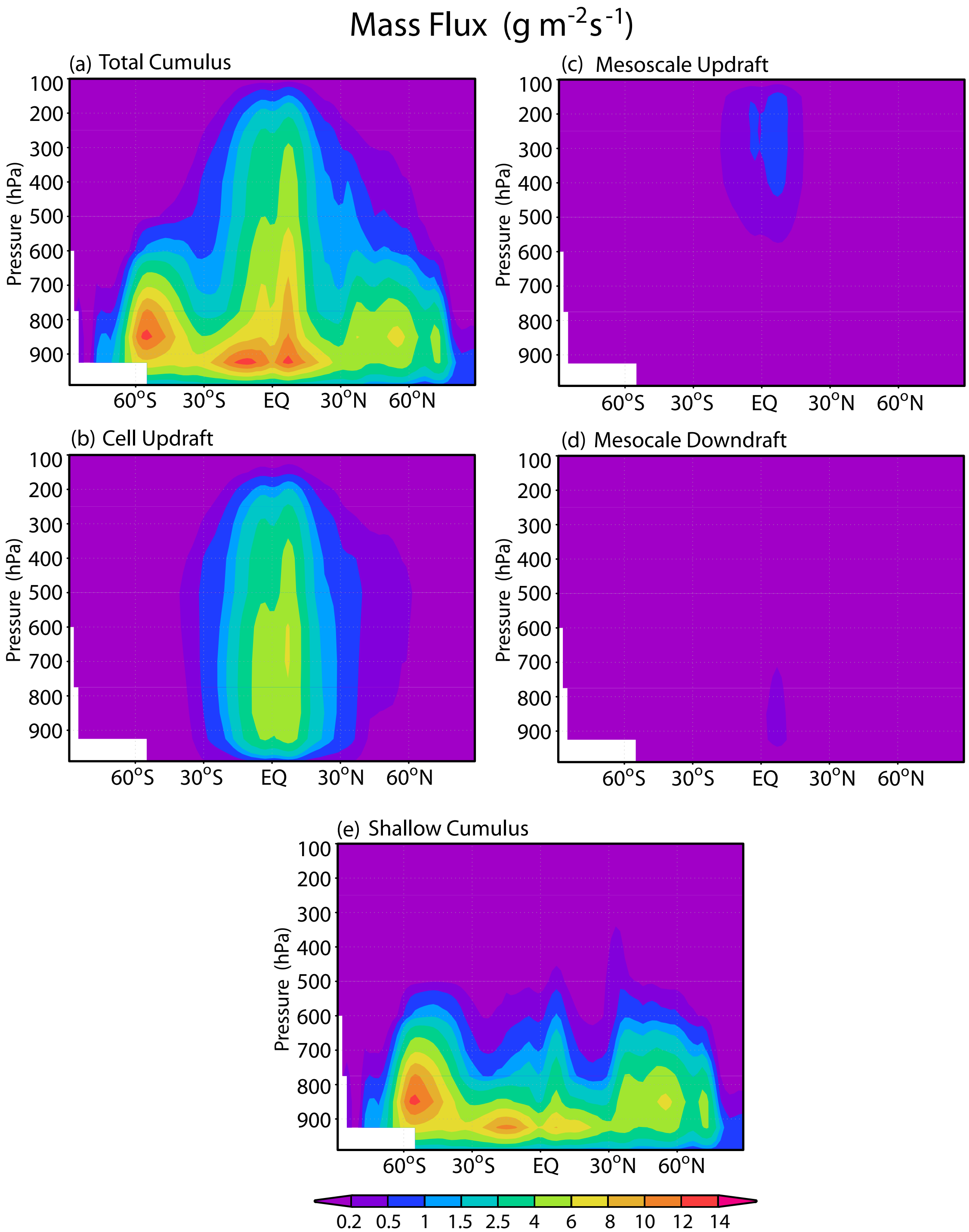


Fig. 1. AM3 annual-mean, zonally averaged cumulus mass fluxes for (a) all convection (except MAA), (b) cell updrafts, (c) mesoscale updrafts, (d) mesoscale downdrafts, and (e) shallow cumulus.

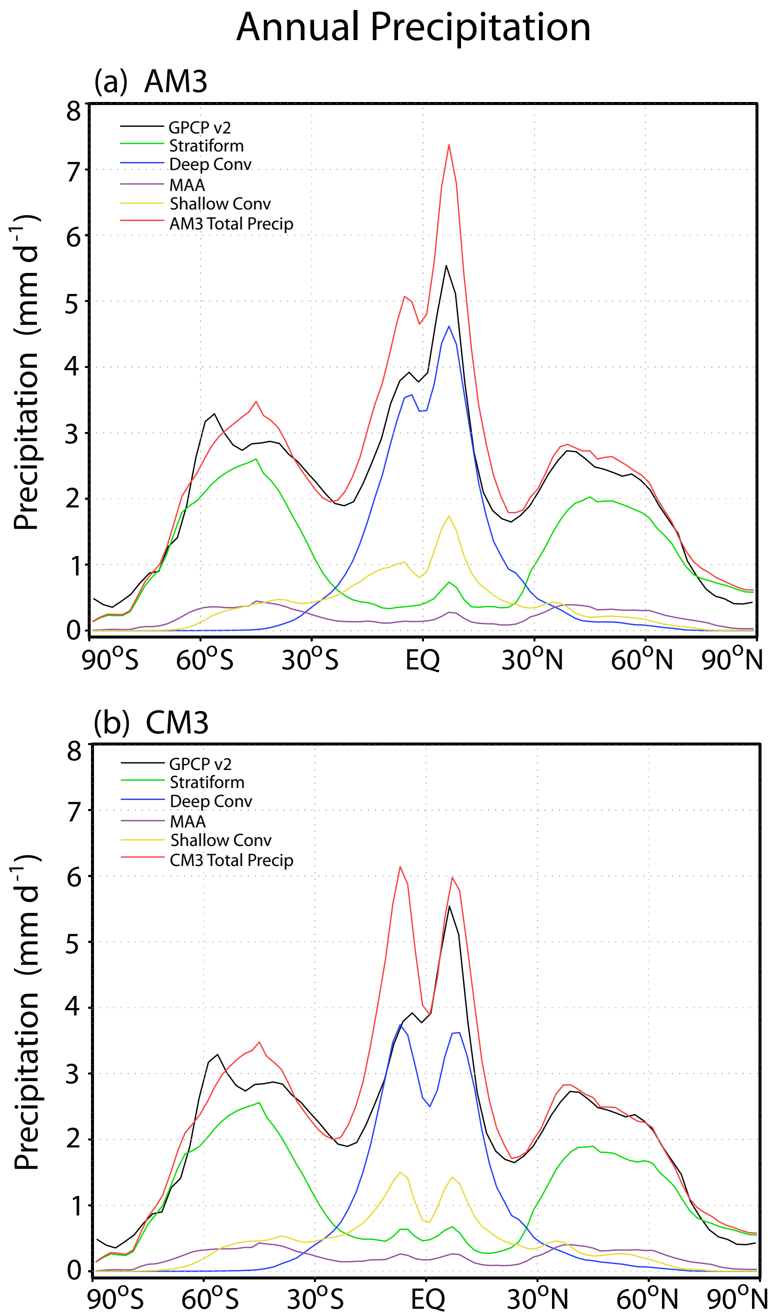


Fig. 2. Annual-mean, zonally averaged precipitation for (a) AM3 and (b) CM3.

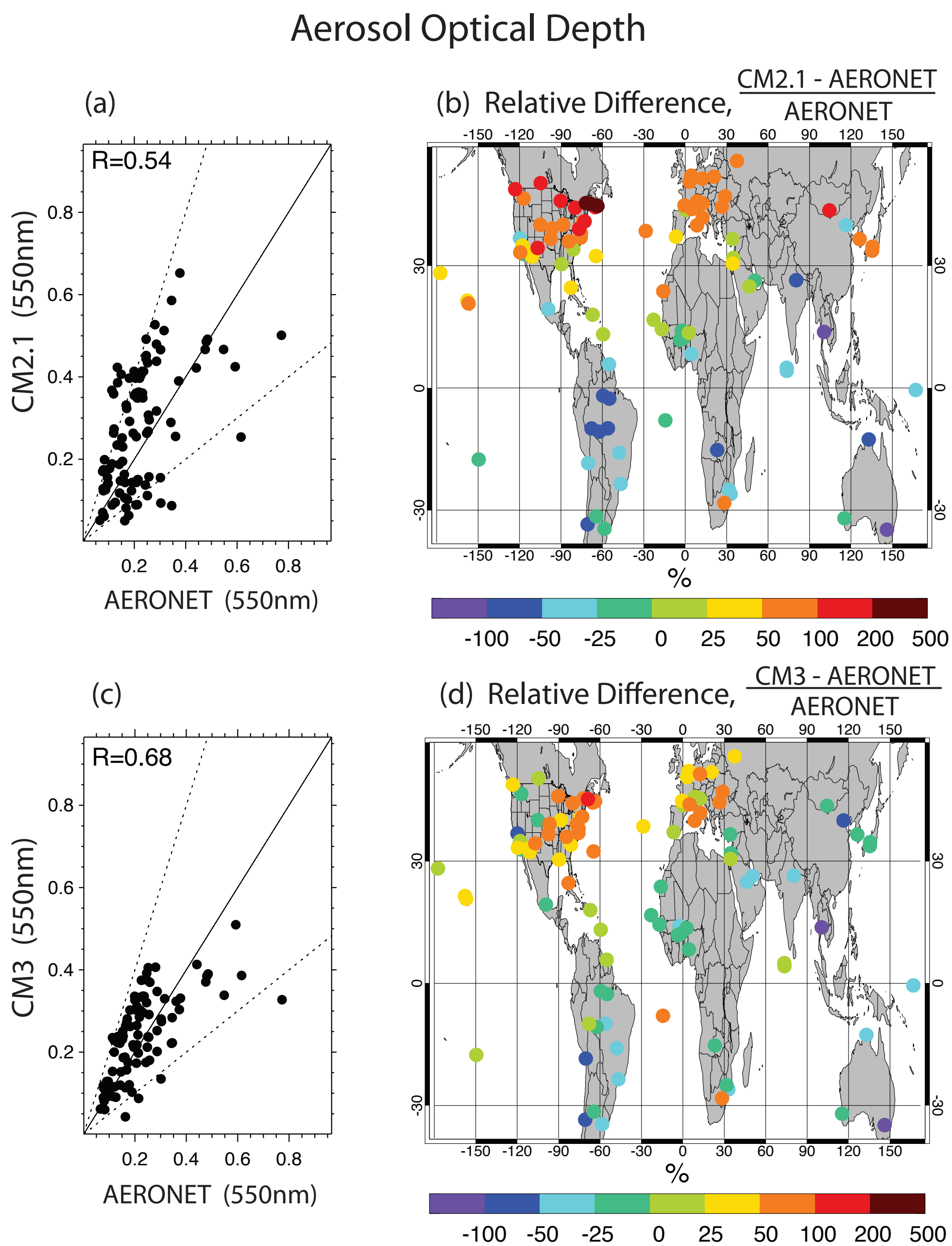


Fig. 3. Climatological aerosol optical depths (550nm) from AERONET and (a), (b) CM2.1 and (c), (d) CM3. Dashed lines in (a) and (c) denote slopes of 0.5 and 2.

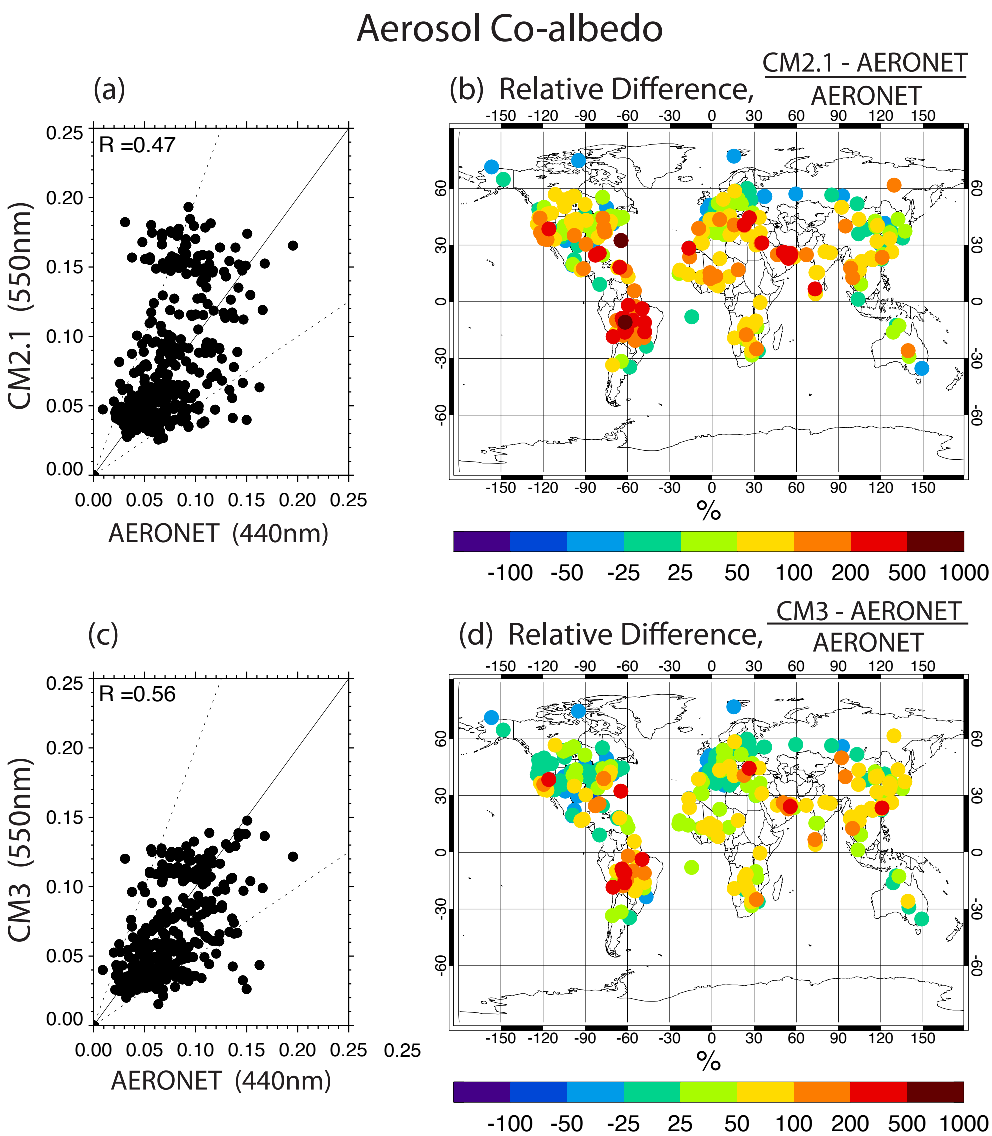


Fig. 4. Climatological aerosol co-albedos from AERONET (440nm) and (a), (b) CM2.1 and (c), (d) CM3 (550nm). Dashed lines in (a) and (c) denote slopes of 0.5 and 2.

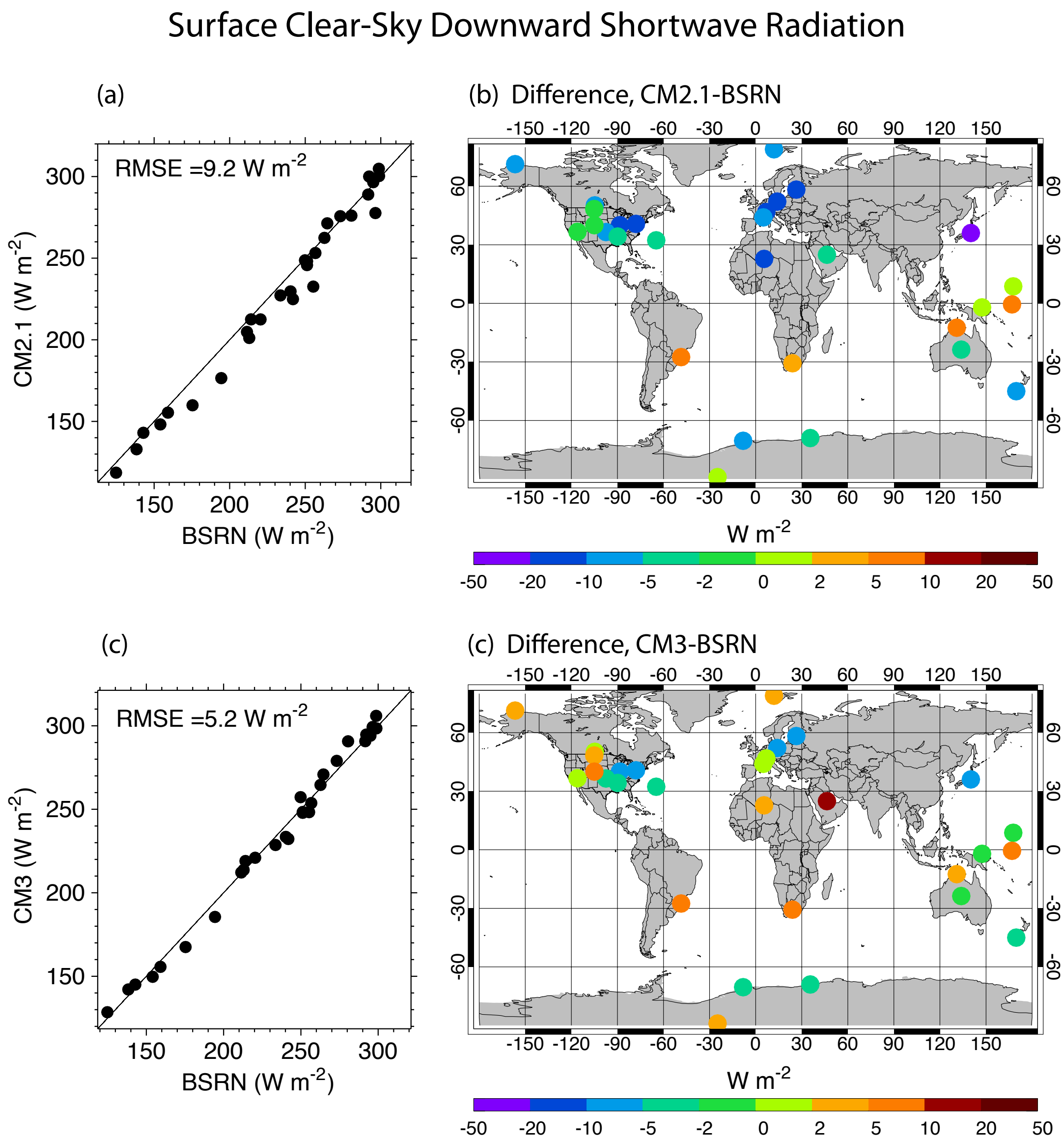


Fig. 5. Surface clear-sky downward shortwave fluxes from BSRN and (a) CM2.1 and (c) CM3. Differences in these fluxes: (b) CM2.1 minus BSRN and (d) CM3 minus BSRN.

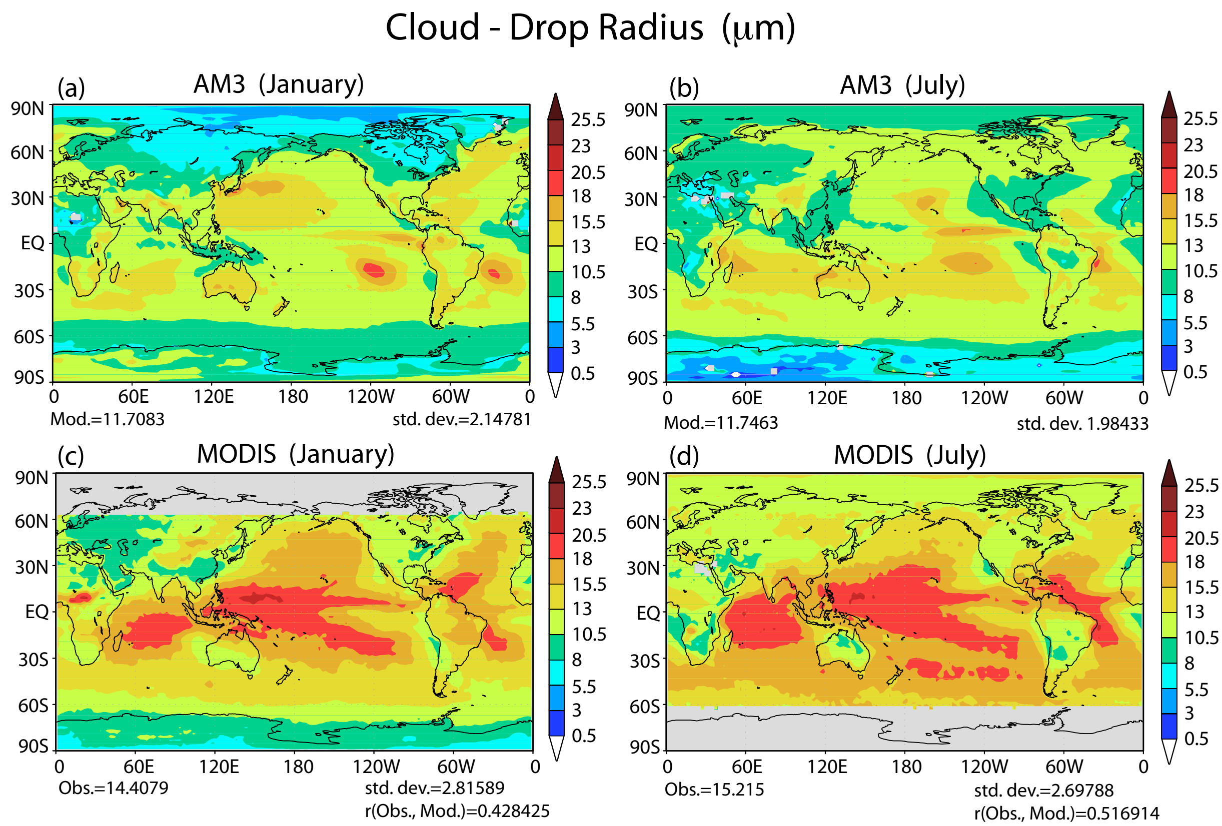


Fig. 6. Cloud-drop radius from MODIS simulator in AM3 for (a) January and (b) July. Cloud-drop radius from MODIS for (c) January and (d) July.

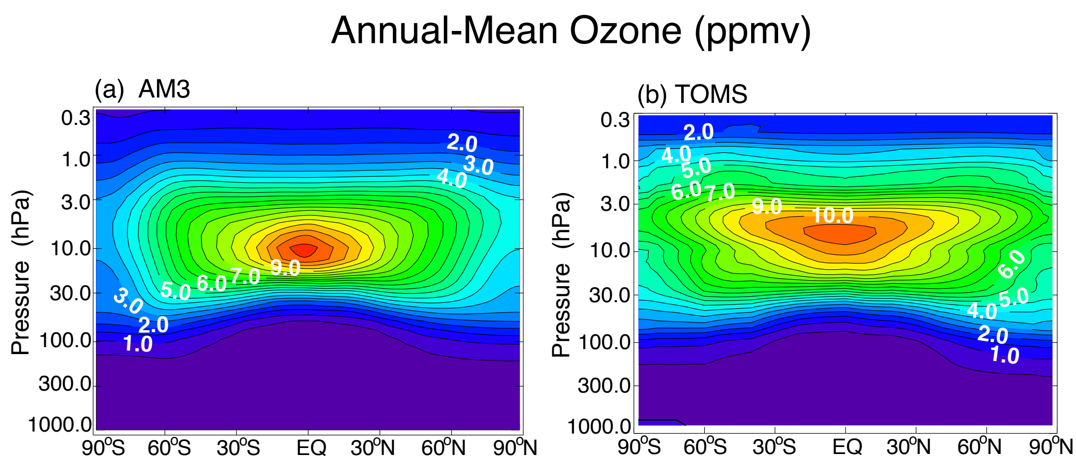


Fig. 7. Annual-mean, zonally averaged ozone from (a) AM3 and (b) TOMS.

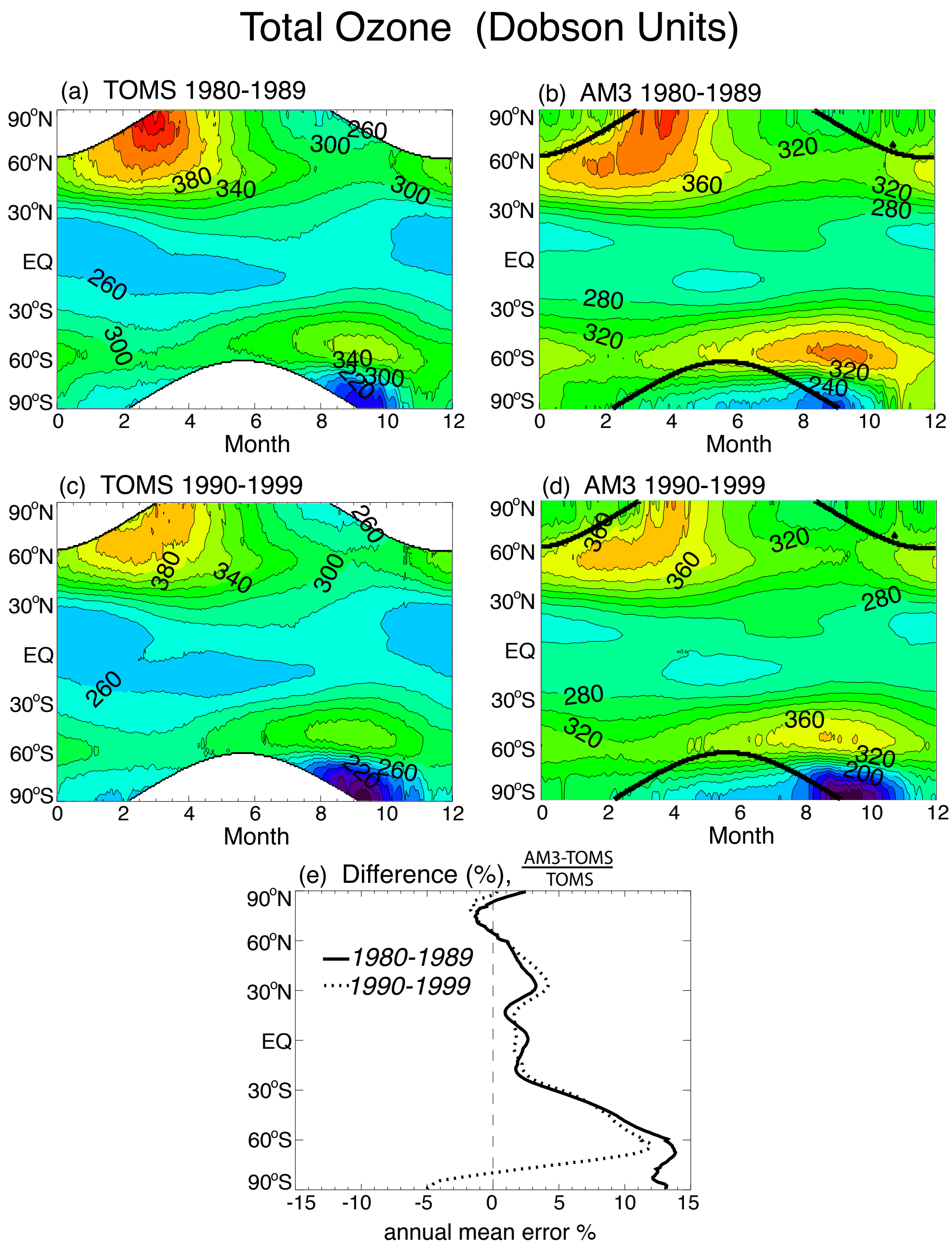


Fig. 8. Vertically integrated, zonally averaged ozone for 1980-1989 from (a) TOMS, (b) AM3 and for 1990-1999 from (c) TOMS, (d) AM3. (e) Annual-mean difference between AM3 and TOMS vertically integrated, zonally averaged ozone.

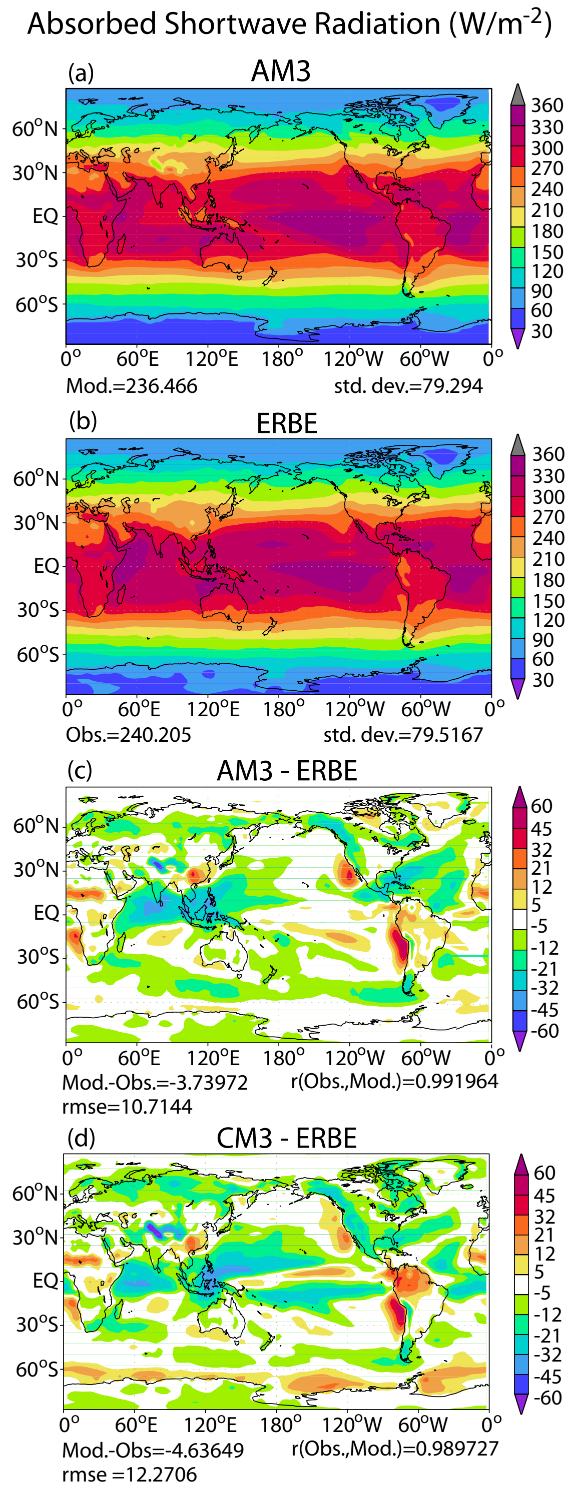


Fig. 9. Annual-mean shortwave absorbed radiation for (a) AM3, (b) ERBE, (c) AM3 minus ERBE, and (d) CM3 minus ERBE.

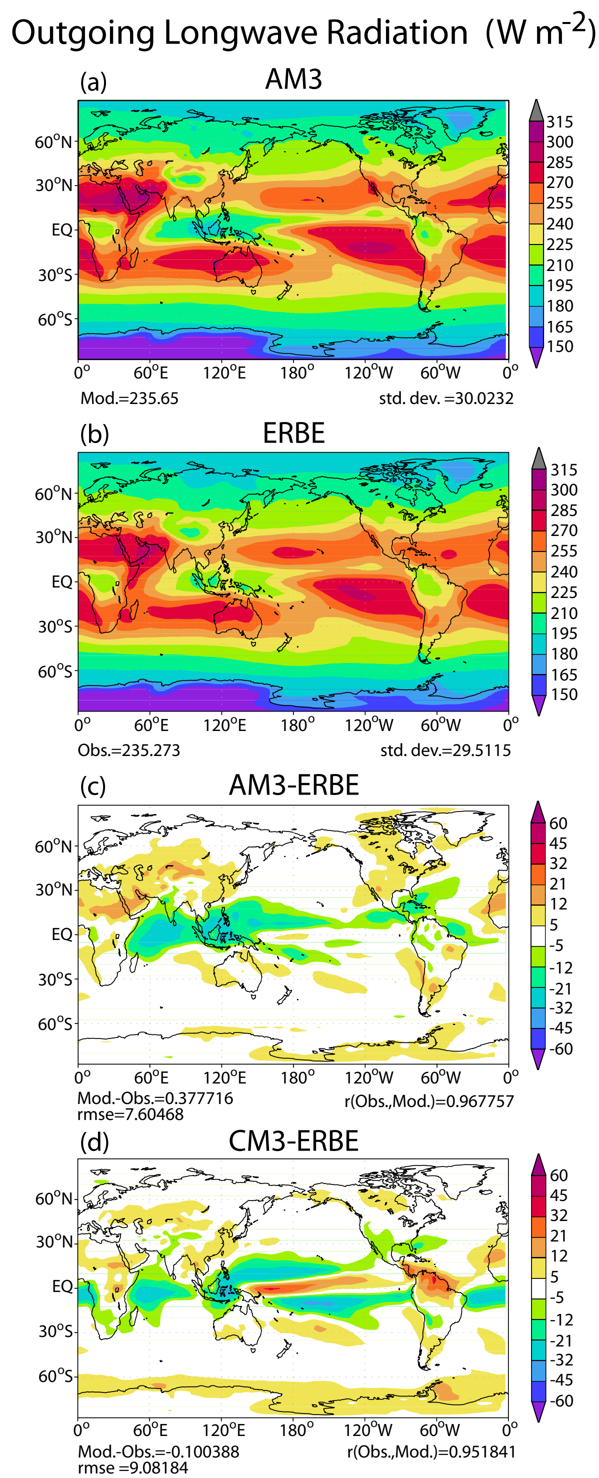


Fig. 10. Annual-mean outgoing longwave radiation for (a) AM3, (b) ERBE, (c) AM3 minus ERBE, and (d) CM3 minus ERBE.

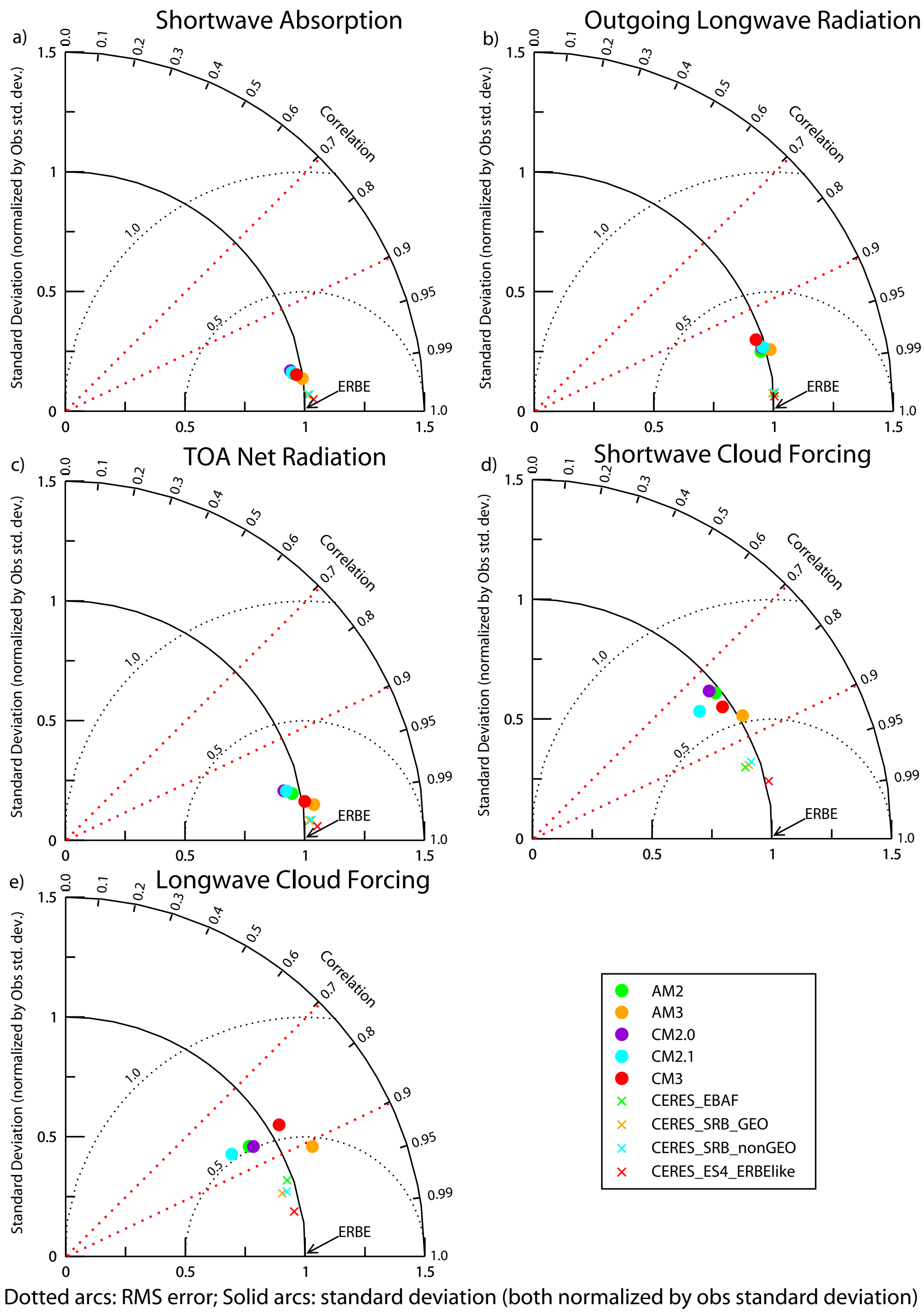


Fig. 11. Taylor diagrams for top-of-atmosphere (TOA) radiation balance. The root-mean-square (RMS) errors, correlations, and standard deviations are based on global, annual means.

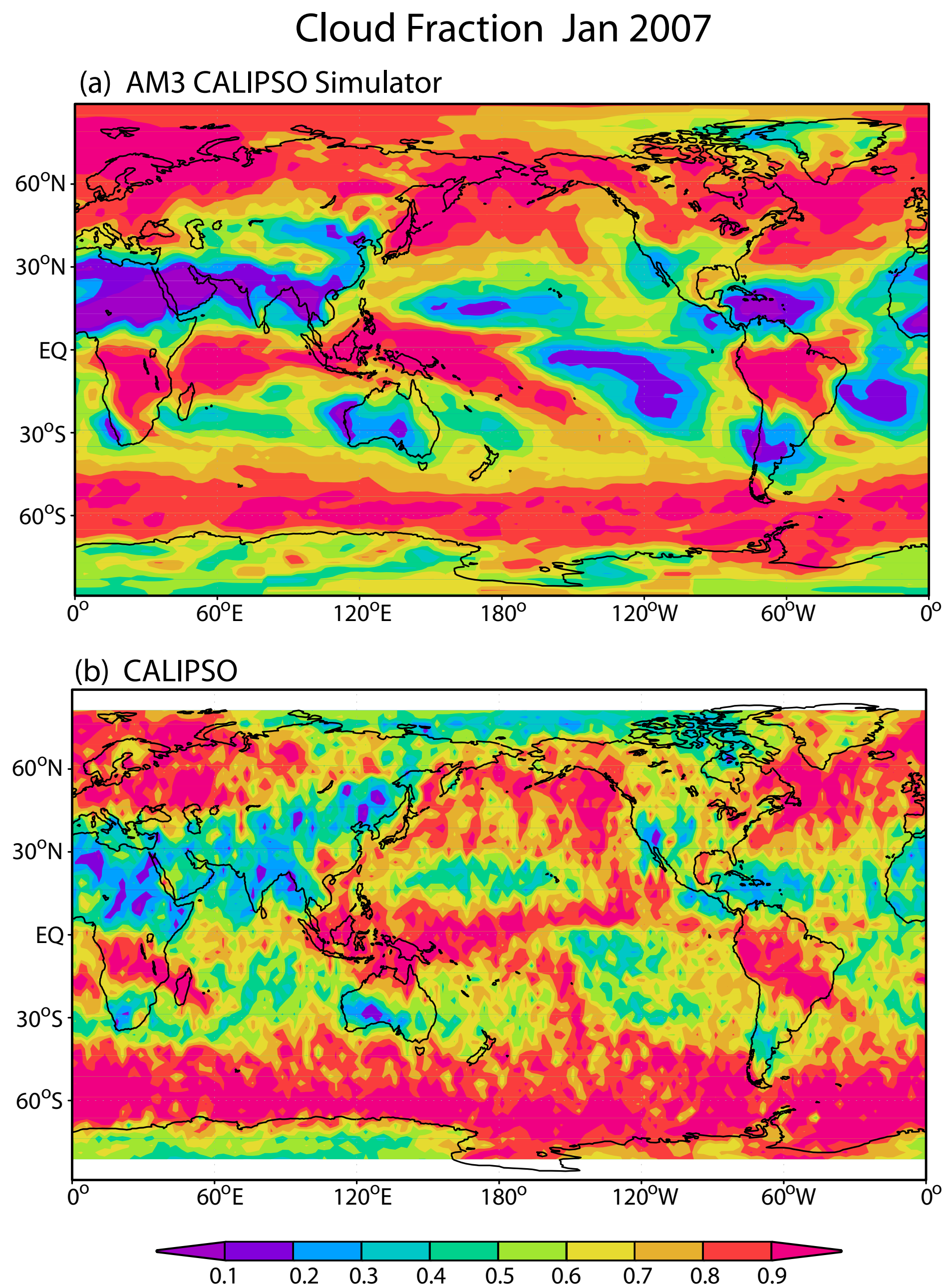


Fig. 12. January 2007 cloud fractions from (a) AM3 CALIPSO simulator and (b) CALIPSO.

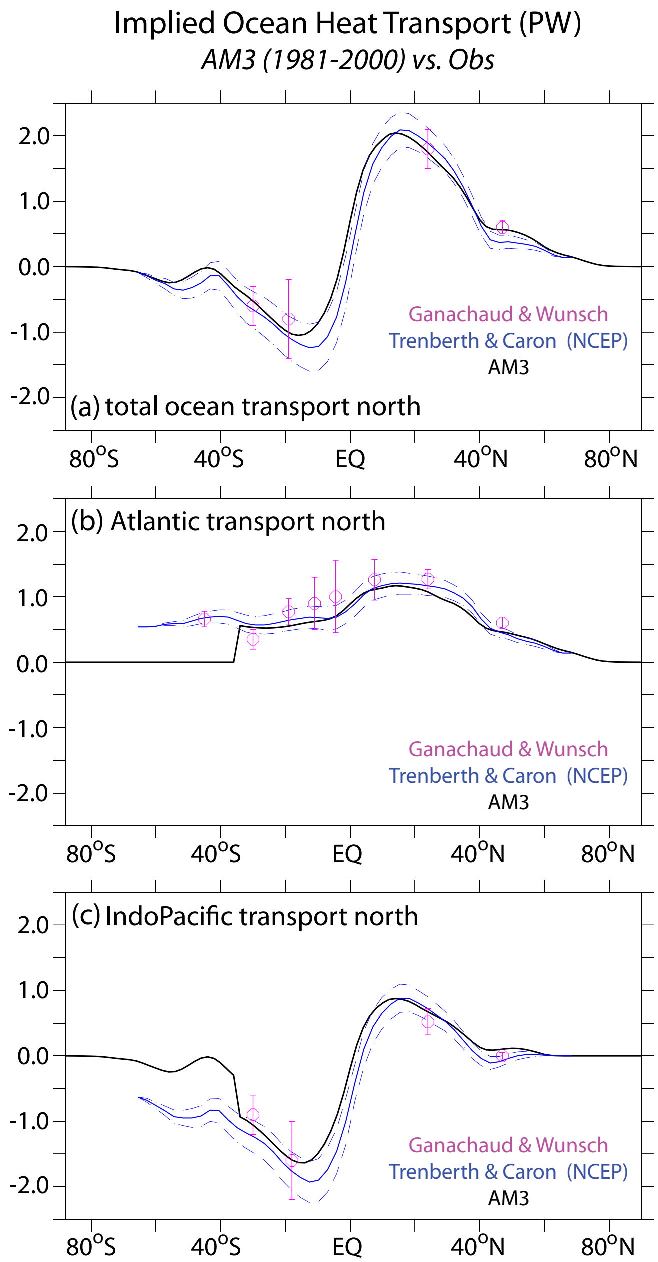


Fig. 13. Implied ocean heat transport for (a) total ocean, (b) Atlantic Ocean, and (c) Indo-Pacific Ocean. Dashed lines and vertical bars indicate range of one standard error above and below Trenberth and Caron (2001) and Ganachaud and Wunsch (2003) estimates, respectively.

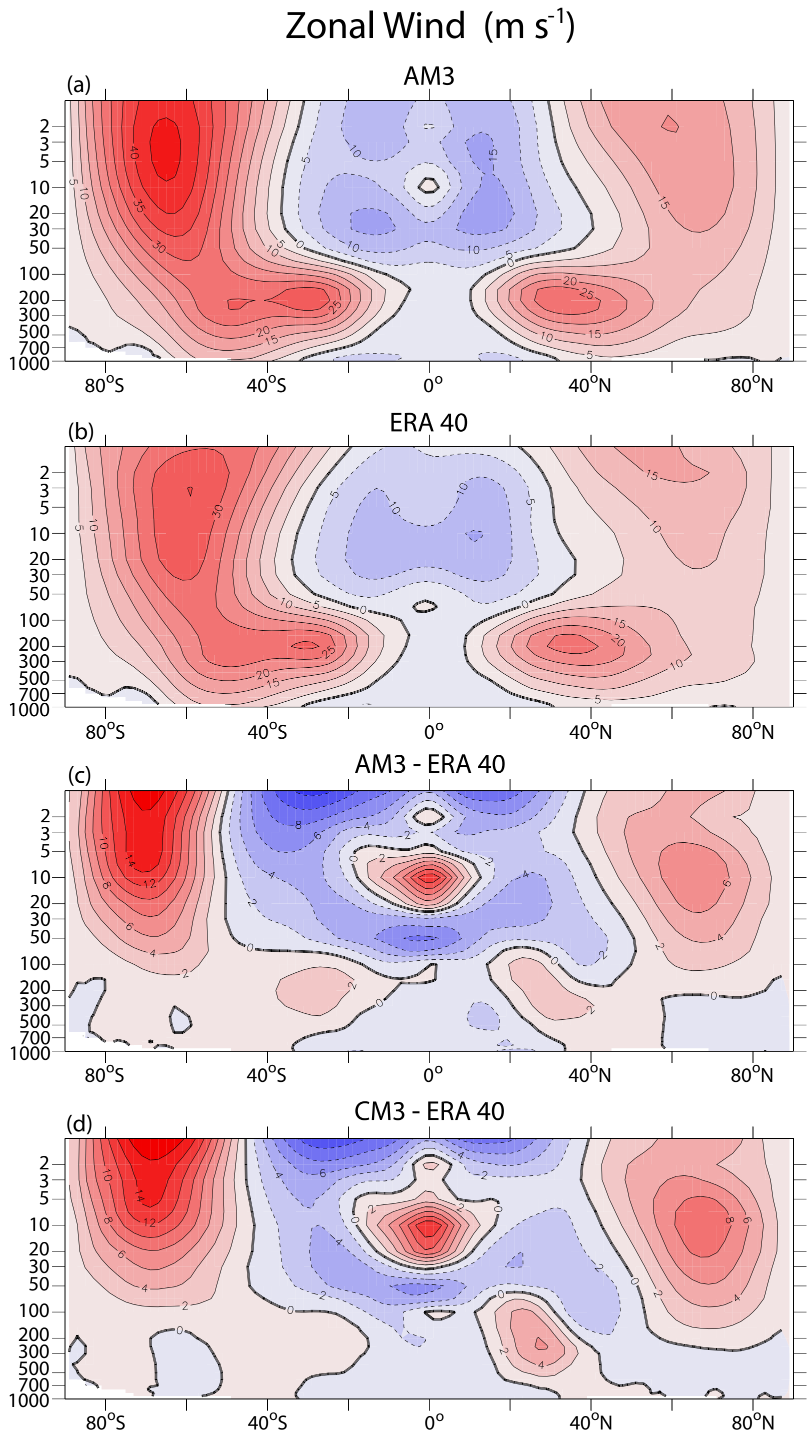


Fig. 14. Annual-mean, zonally averaged zonal wind for (a) AM3, (b) ERA-40, (c) AM3 minus ERA-40, and (d) CM3 minus ERA-40.

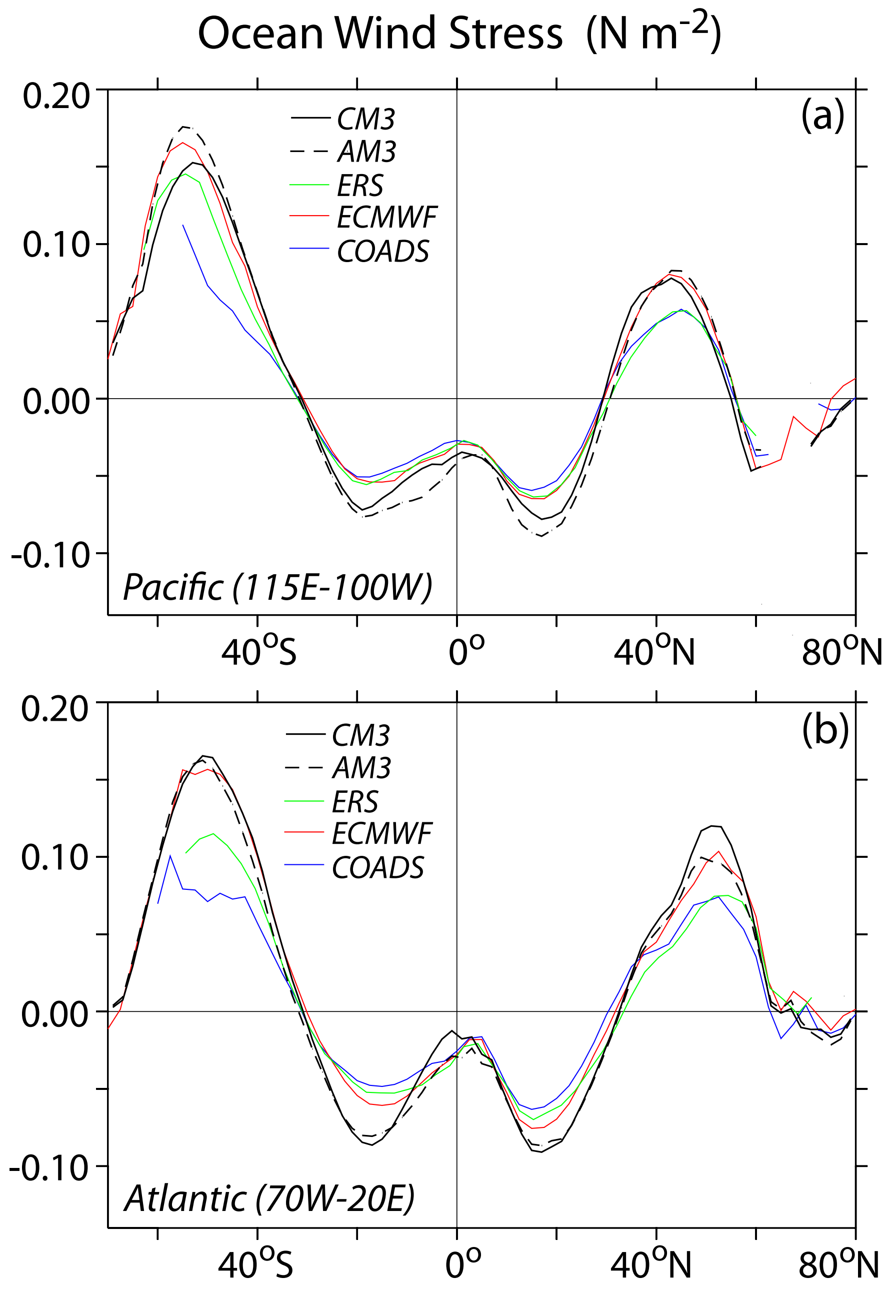


Fig. 15. Annual-mean wind stress for (a) Pacific Ocean and (b) Atlantic Ocean.

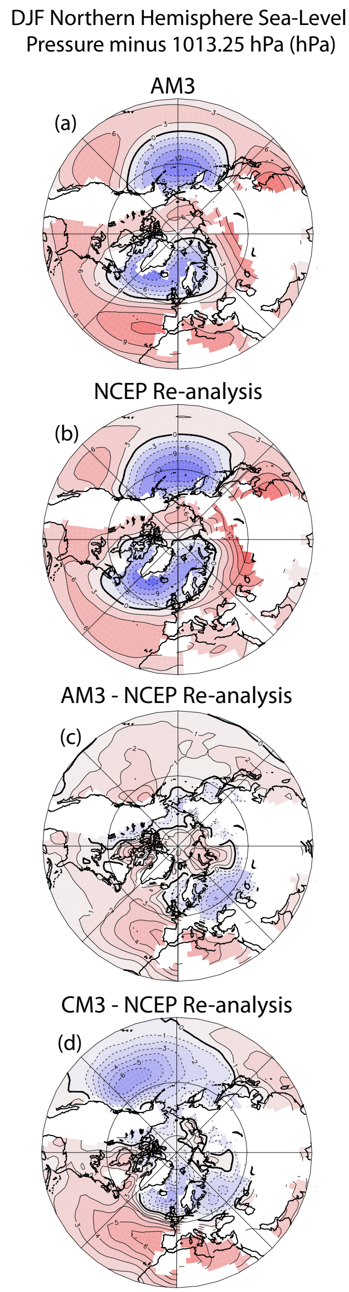


Fig. 16. Northern Hemisphere DJF sea-level pressure minus 1013.25 hPa for (a) AM3, (b) NCEP re-analysis, (c) AM3 minus NCEP re-analysis, and (d) CM3 minus NCEP re-analysis. Contour intervals: (a), (b) 3 hPa; (c) , (d) 1 hPa. Areas with mean surface pressures less than 950 hPa are masked.

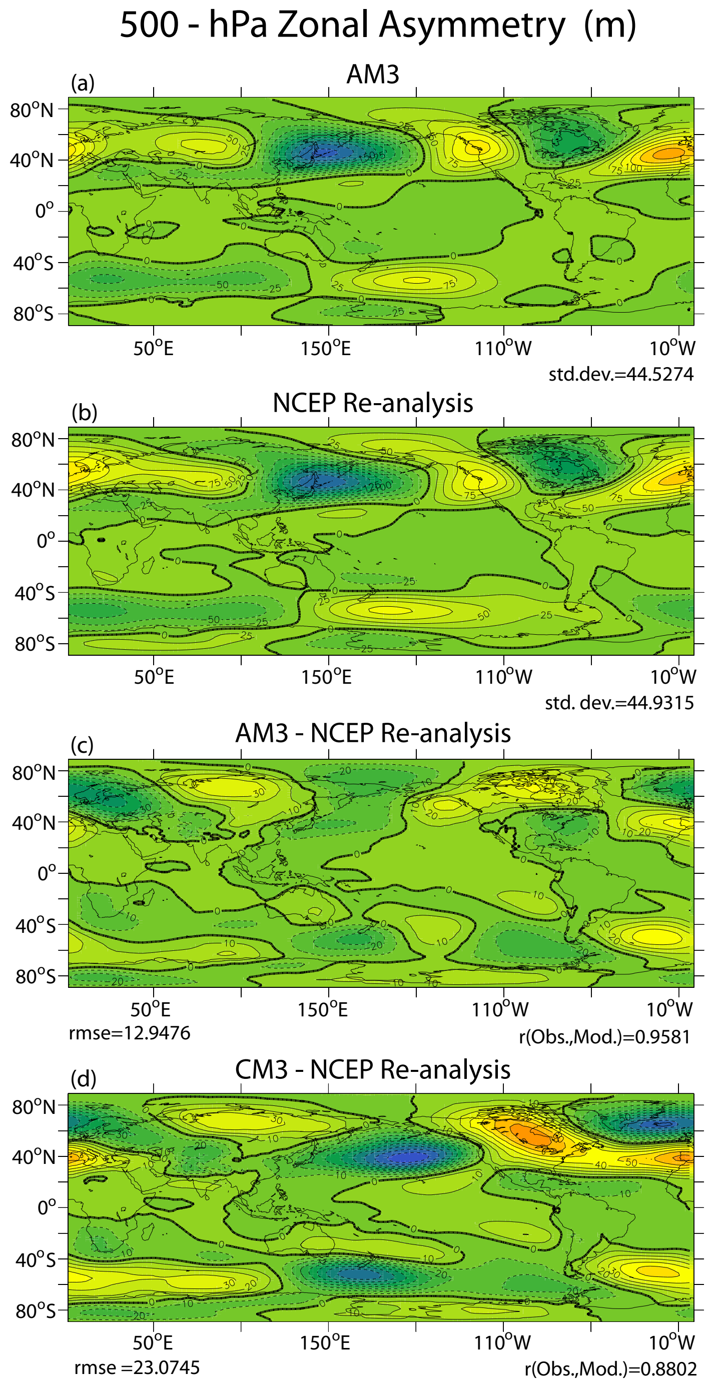


Fig. 17. DJF departure from zonally averaged 500-hPa geopotential height for (a) AM3, (b) NCEP re-analysis, (c) AM3 minus NCEP re-analysis, and (d) CM3 minus NCEP re-analysis.

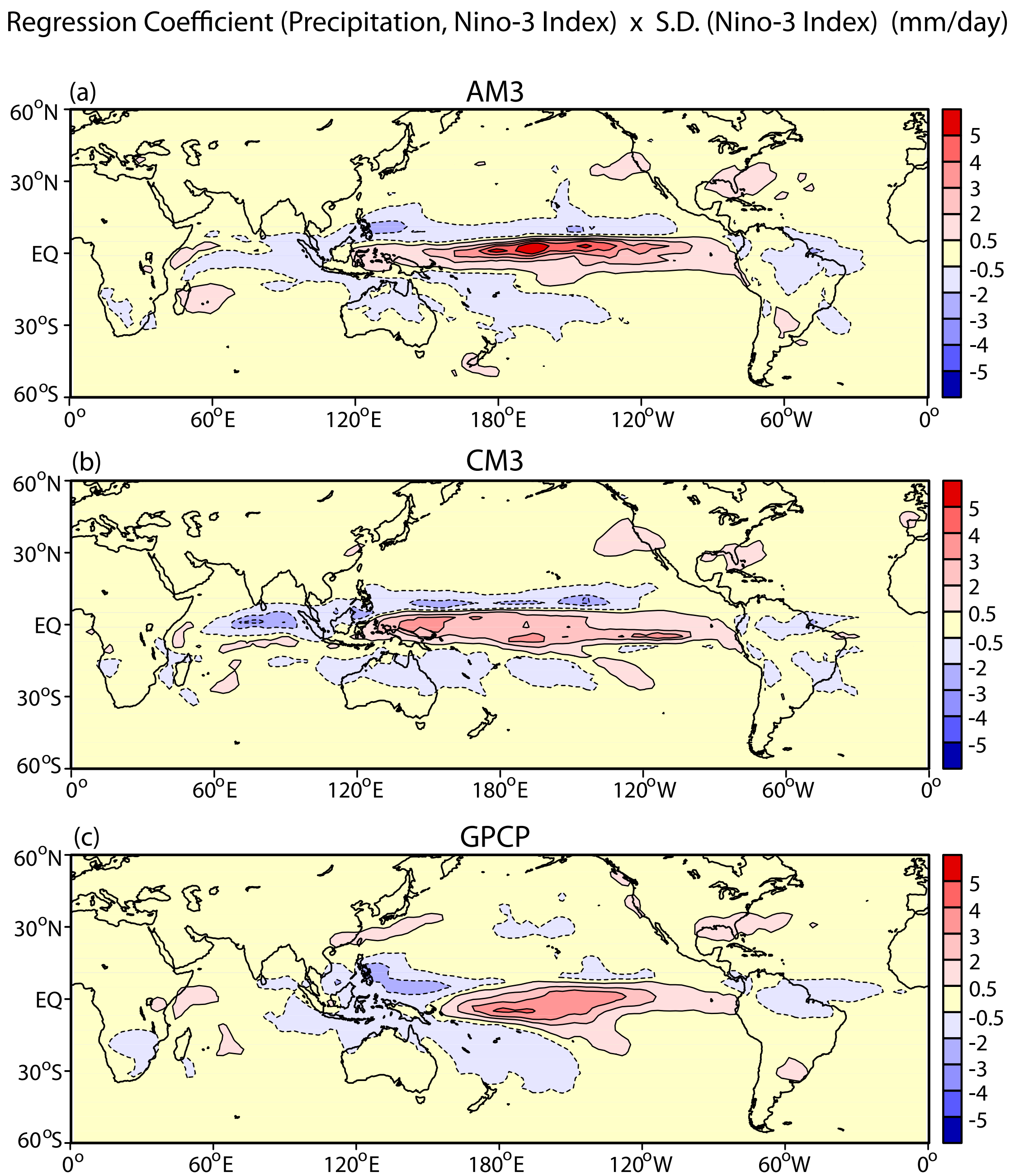


Fig. 18. DJF product of the standard deviation of the Niño-3 index and regression coefficient between precipitation and Niño-3 index for (a) AM3, (b) CM3, and (c) GPCP.

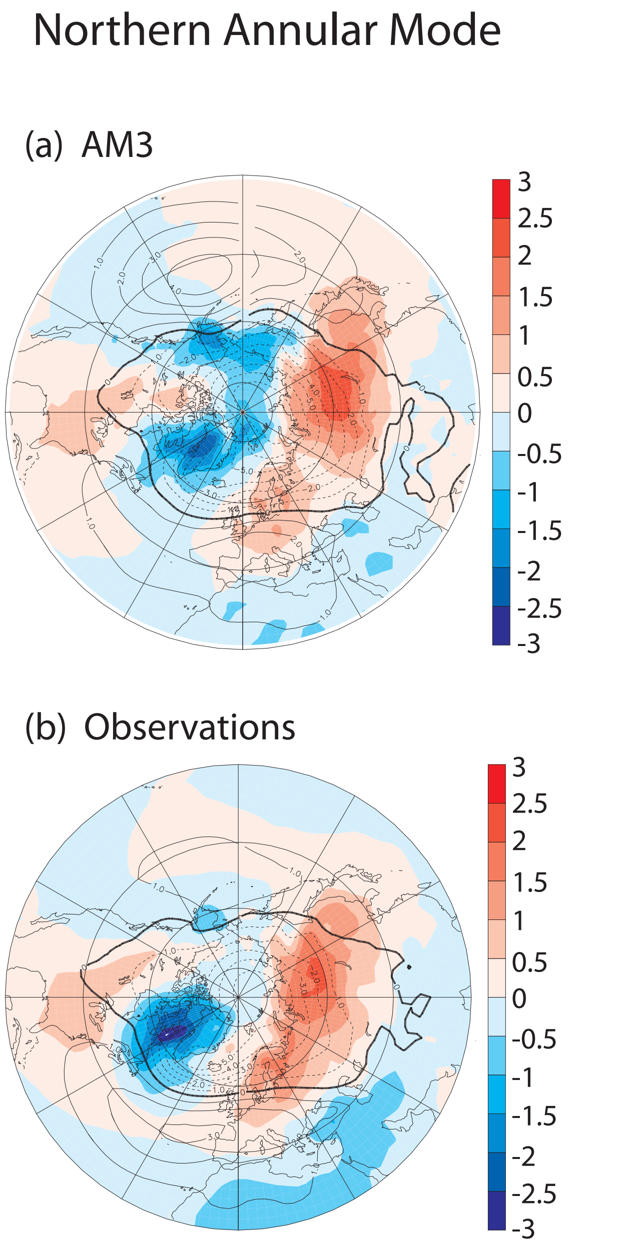


Fig. 19. Product of the standard deviation of the NAM index and regression coefficients between the NAM index and SLP (contours, hPa) and 2-m temperature (shading, $^{O}$C) for (a) AM3 and (b) NCEP re-analysis.

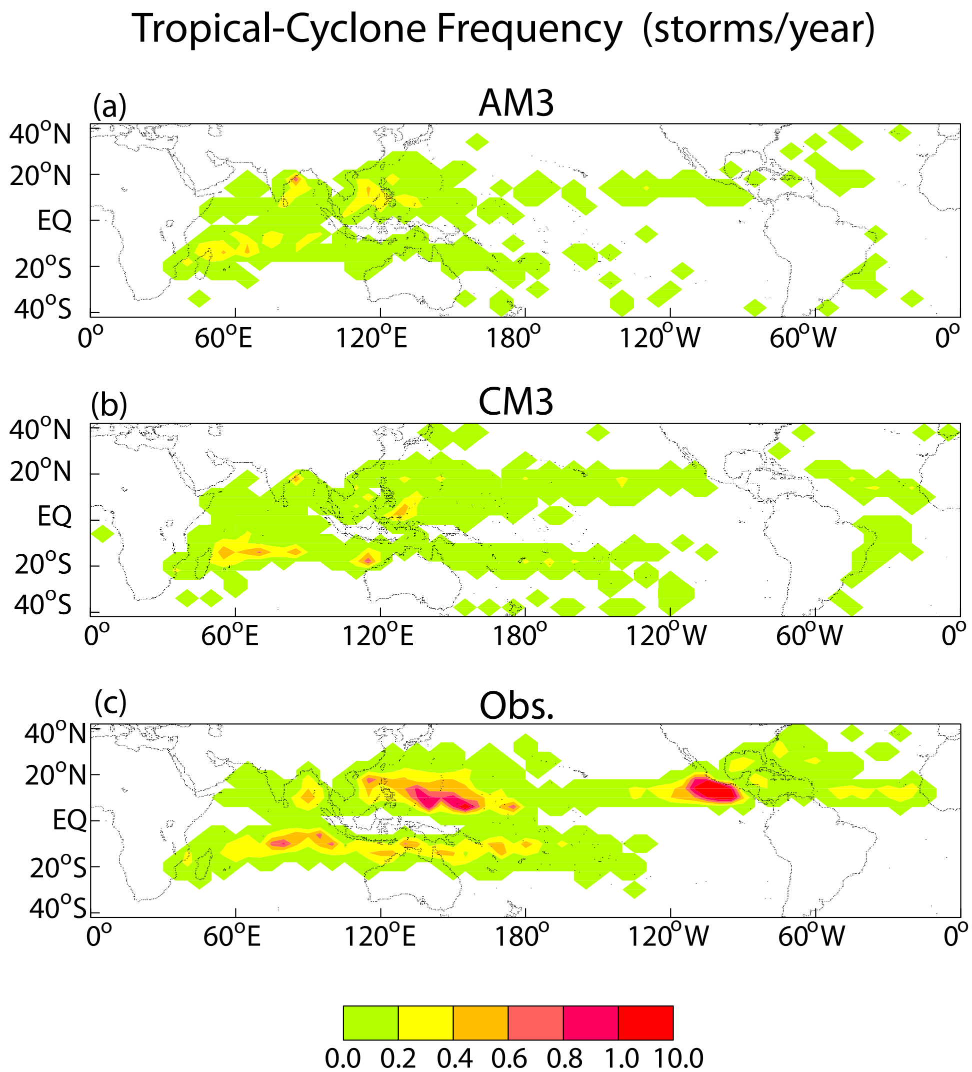


Fig. 20. Tropical-cyclone frequency for (a) AM3, (b) CM3, (c) U.S. National Hurricane Center and Navy observations.

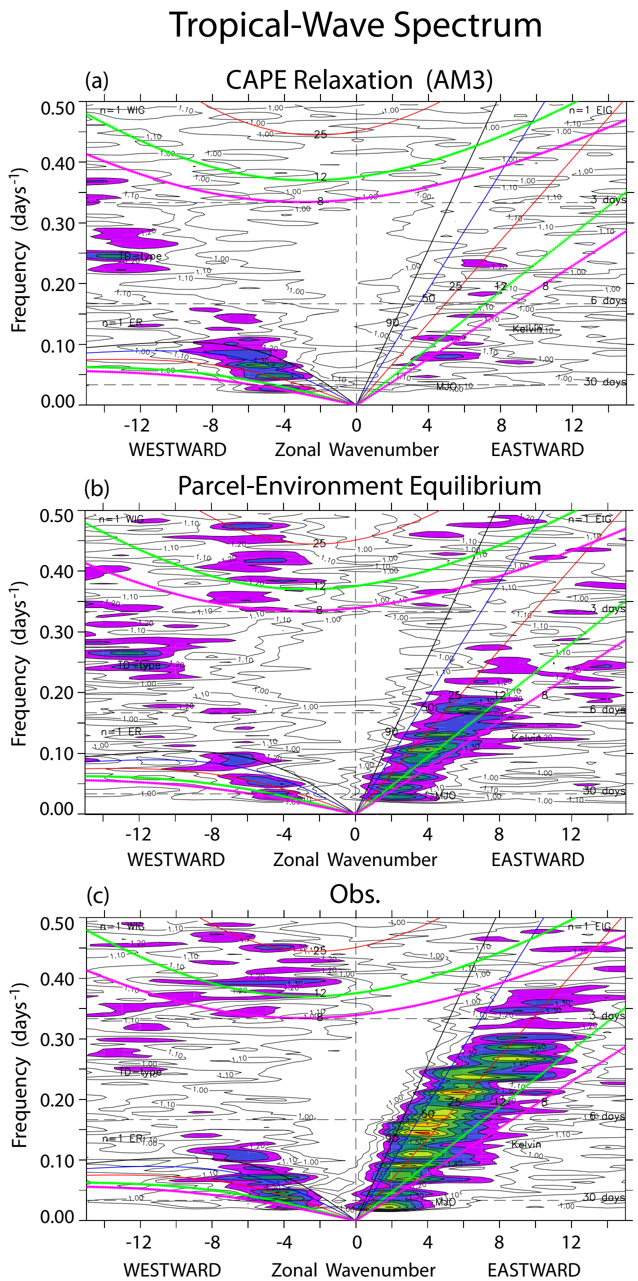


Fig. 21. Normalized tropical symmetric OLR wavenumber-frequency power spectrum for (a) AM3, (b) AM3 with CAPE relaxation closure for deep cumulus replaced by a closure in which CAPE tendencies in the environment of cumulus parcels are balanced by deep convection with low-level-lift trigger, and (c) OLR observations. Contour interval is .1 (shown for values 1.0 and greater) with colored shading of regions greater than 1.2 indicating power associated with MJO, Kelvin and other tropical convective waves that are significantly above an approximately red-noise background power spectra. The colored lines represent various equatorial wave dispersion curves labeled for five different equivalent depths, i.e., 8, 12, 25, 50 and 90m.

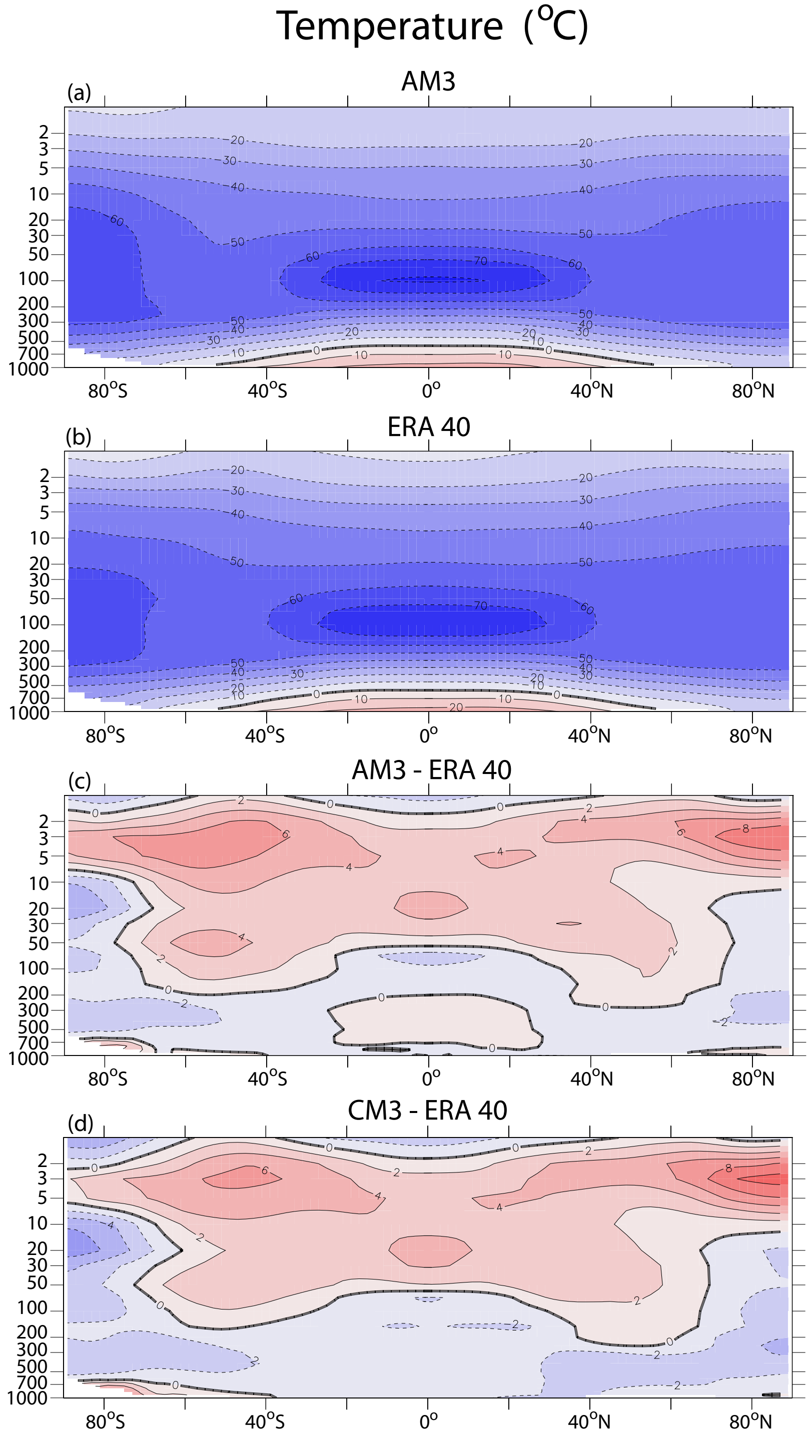


Fig. 22. Annual-mean, zonally averaged temperature for (a) AM3, (b) ERA-40 re-analysis, (c) AM3 minus ERA-40, and (d) CM3 minus ERA-40.

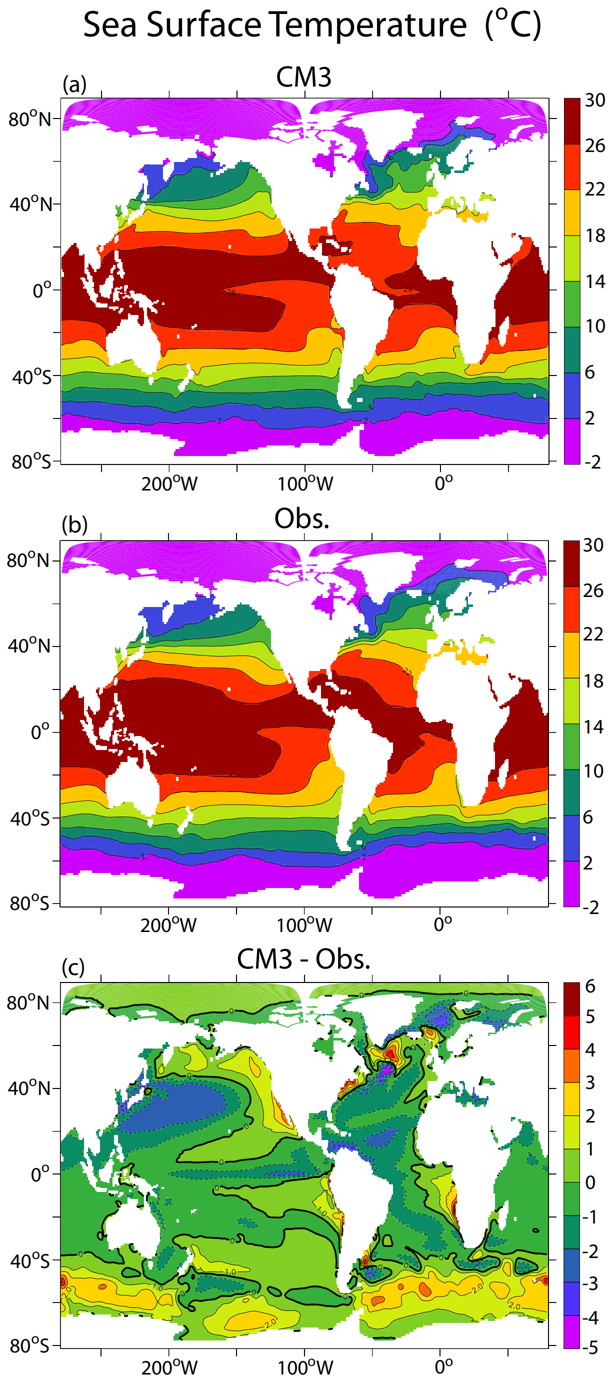


Fig. 23. Sea-surface temperatures for (a) CM3, (b) observations compiled at Lawrence Livermore National Laboratory (http://www-pcmdi.llnl.gov/projects/amip/AMIP2EXPDSN/BCS_OBS/amip2_bcs.htm), and (c) difference.

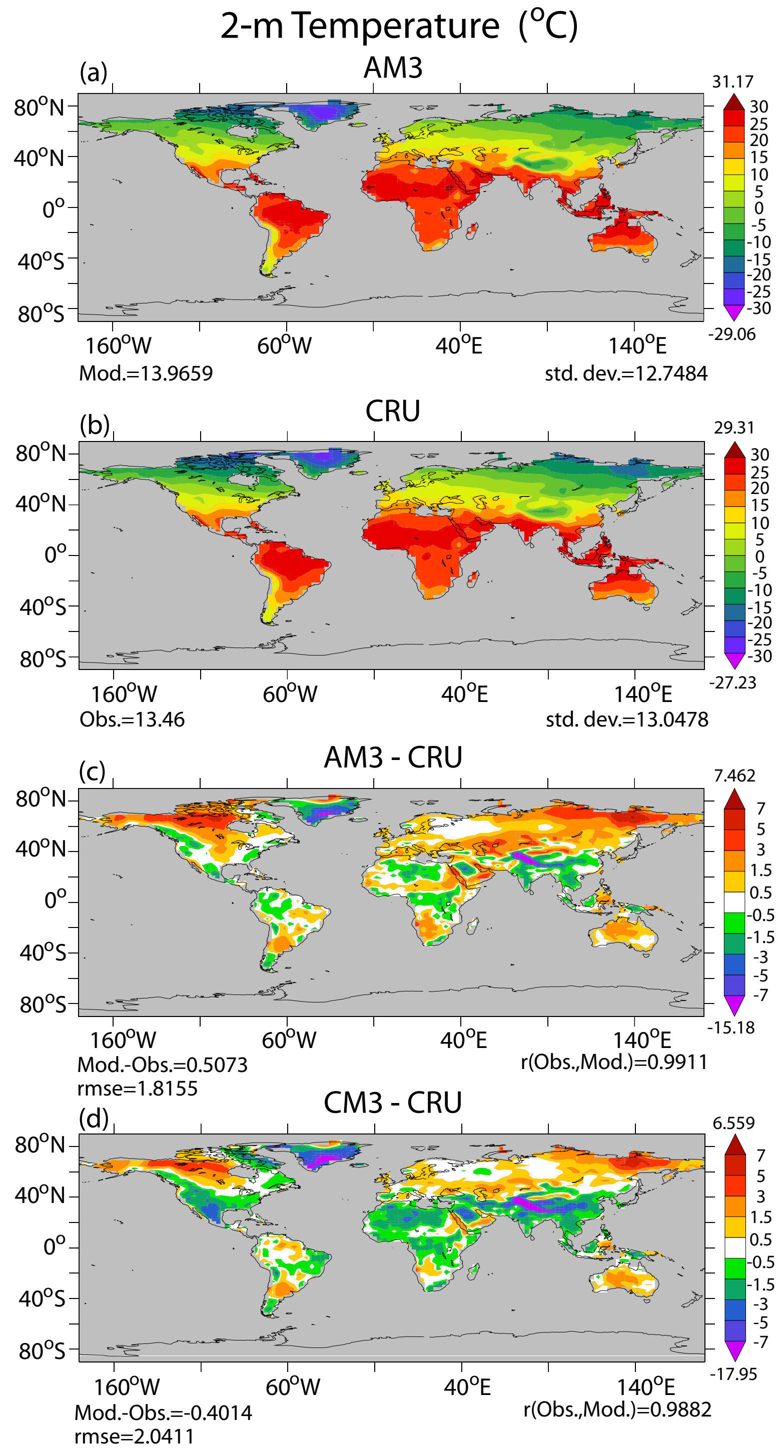


Fig. 24. 2-m temperatures for (a) AM3, (b) CRU, (c) AM3 minus CRU, and (d) CM3 minus CRU.

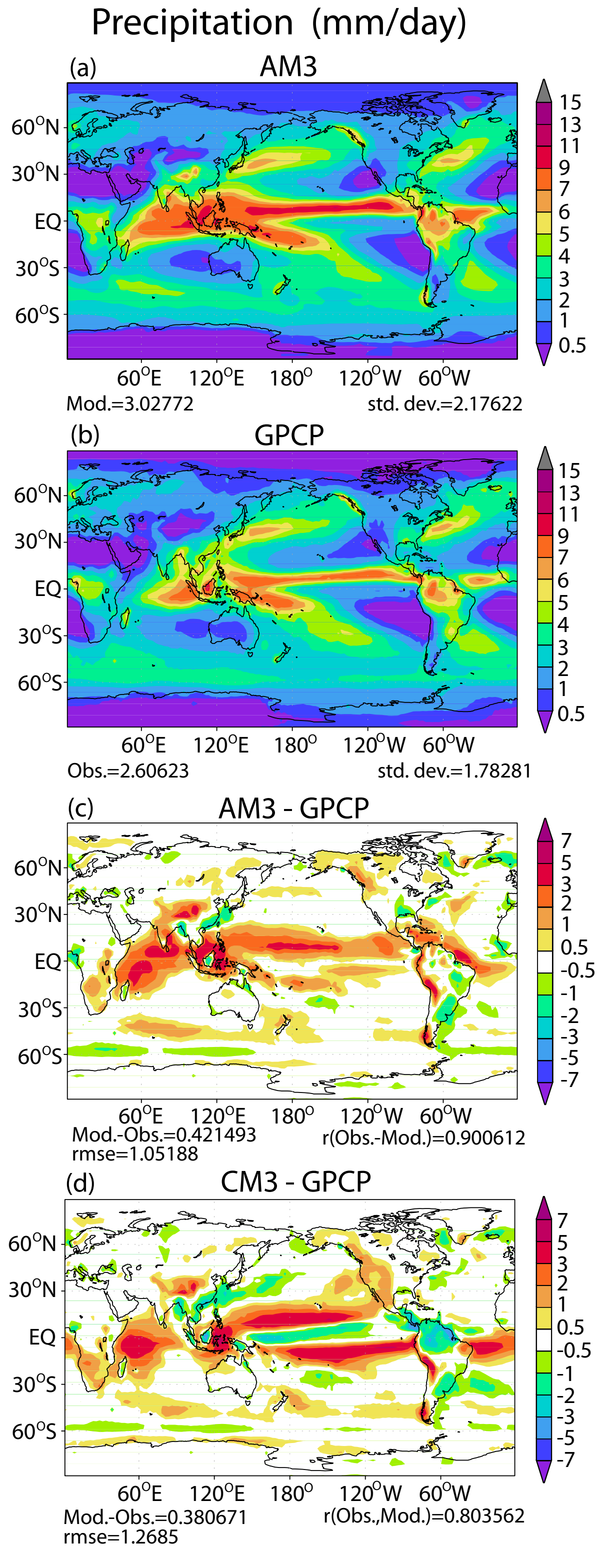


Fig. 25. Annual-mean precipitation for (a) AM3, (b) GPCP v. 2, (c) AM3 minus GPCP v. 2, and (d) CM3 minus GPCP v. 2.

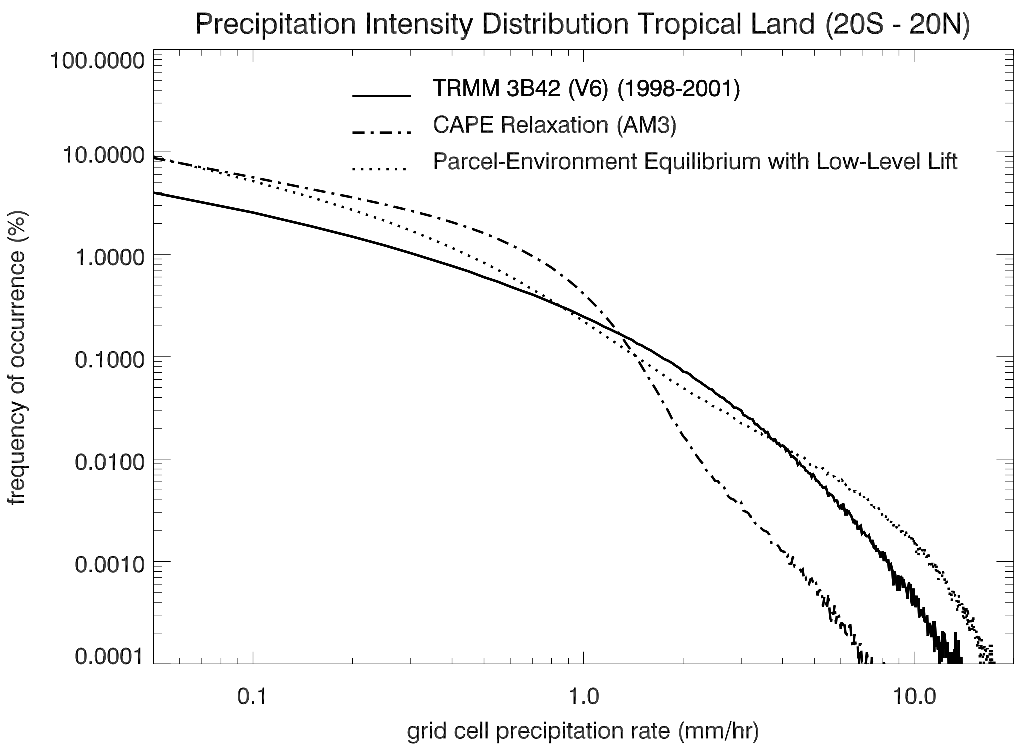


Fig. 26. Precipitation intensity distribution from TRMM, AM3, and AM3 with CAPE relaxation closure for deep cumulus replaced by a closure in which CAPE tendencies in the environment of cumulus parcels are balanced by deep convection with low-level-lift trigger.

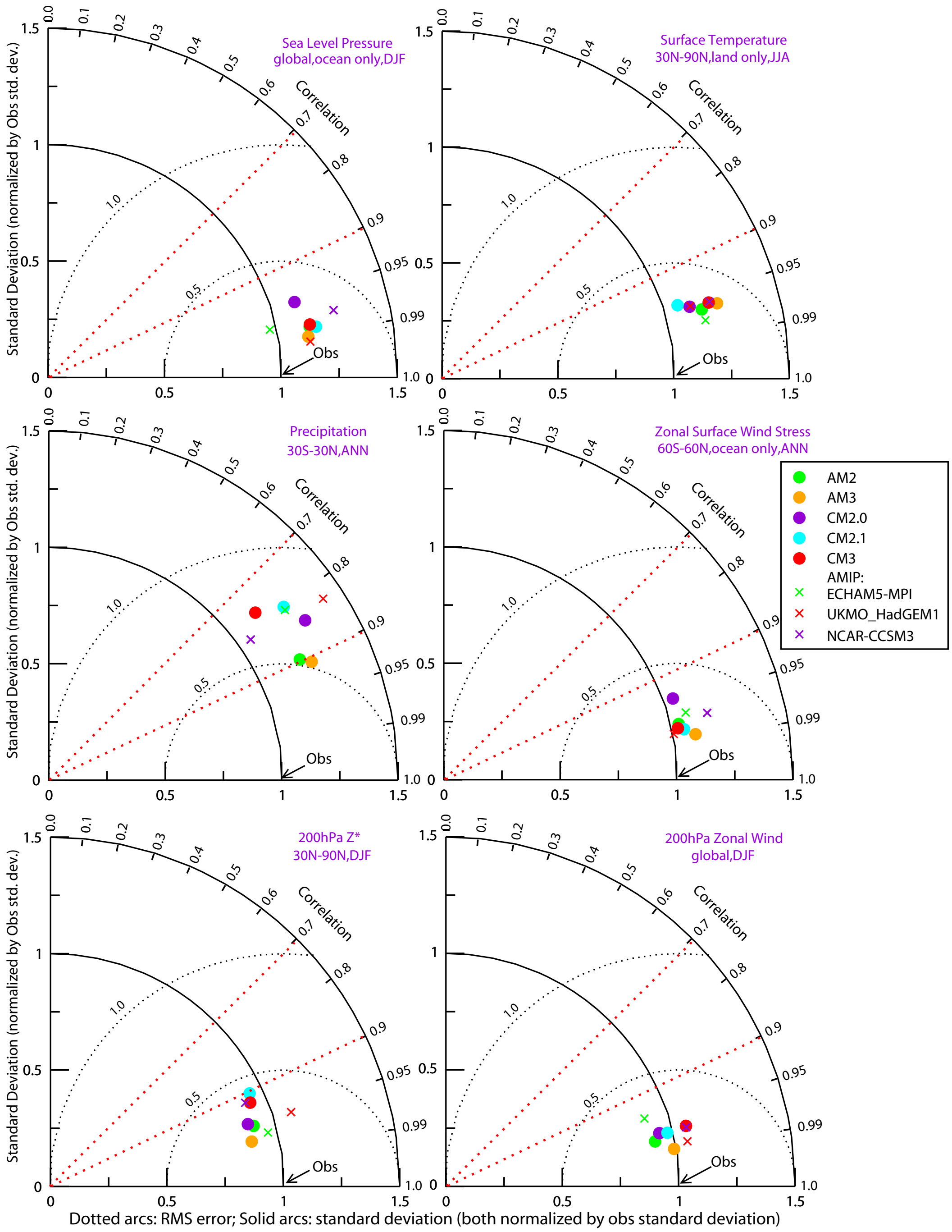


Fig. 27. Taylor diagrams for sea-level pressure, surface temperature, precipitation, zonal surface wind stress, 200 hPa deviation of geopotential height from zonal mean, and 200 hPa zonal wind. Regions and periods for averages as indicated. The ECHAM5-MPI, UKMO_HadGEM1, and NCAR-CCSM3 results are their latest AMIP submissions to the World Climate Research Program's CMIP3. Observations of sea-level pressure, geopotential height, and winds from NCEP re-analysis; precipitation from GPCP v. 2; surface temperature from CRU; and wind stress from ERA-40.

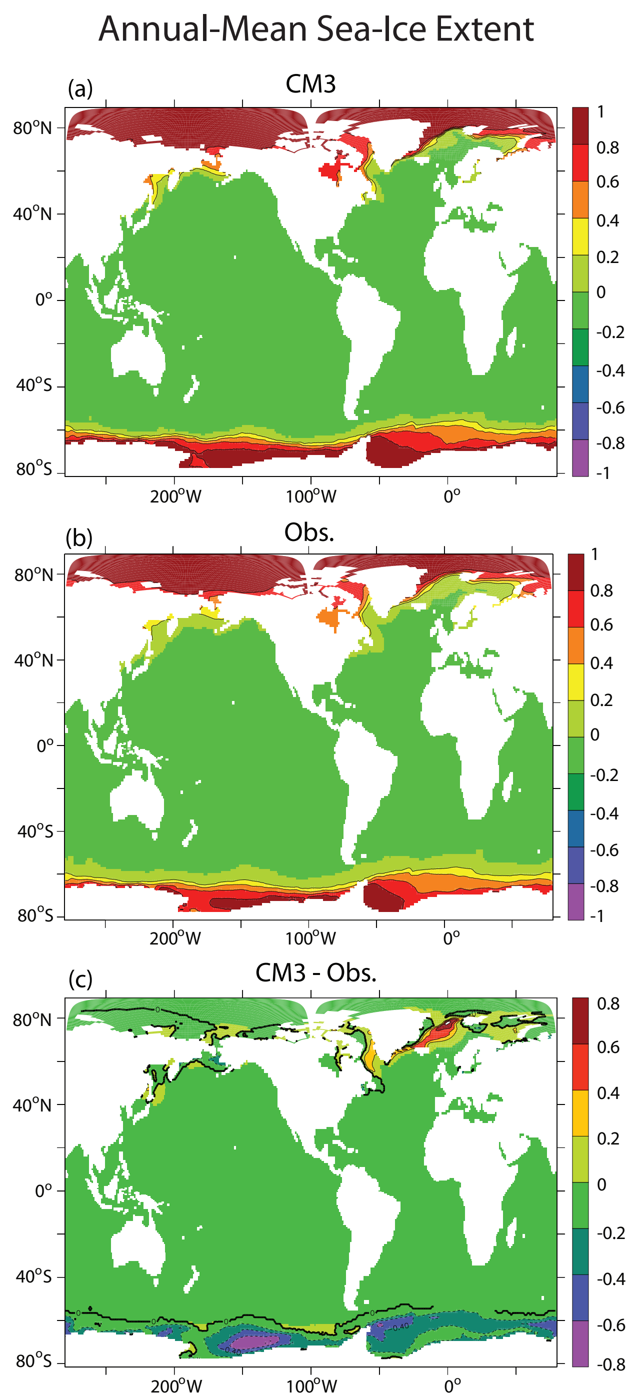


Fig. A1. Annual-mean sea-ice extent for (a) CM3, (b) observations, and (c) difference. Sea-ice extent is defined to be 1 if sea-ice concentration is 15% or greater and 0 otherwise. Observed ice extent is computed from monthly ice concentrations following Hurrell et al. (2008). Values between 0 and 1 result from time averaging.

**Table 1. Coefficients $a_k$ and $b_k$ for calculation of interface pressures using $p = a_k + b_k \times p_s$, where $p$ is pressure and $p_s$ is surface pressure (Simmons and Burridge, 1981). Pressures and heights of interface levels corresponding to a scale height of 7.5 km and $p_s$ = 1013.25 hPa are also shown.**

| $k$ | $a_k$ (Pa) | $b_k$ | $p$(hPa) | $z$ (km) |
|---|---|---|---|---|
| 1 | 1 | 0 | 0.01 | 86.45 |
| 2 | 2.6972 | 0 | 0.03 | 79.00 |
| 3 | 5.1714 | 0 | 0.05 | 74.12 |
| 4 | 8.8946 | 0 | 0.09 | 70.05 |
| 5 | 14.248 | 0 | 0.14 | 66.52 |
| 6 | 22.072 | 0 | 0.22 | 63.24 |
| 7 | 33.613 | 0 | 0.34 | 60.08 |
| 8 | 50.481 | 0 | 0.50 | 57.03 |
| 9 | 74.800 | 0 | 0.75 | 54.08 |
| 10 | 109.40 | 0 | 1.09 | 51.23 |
| 11 | 158.00 | 0 | 1.58 | 48.48 |
| 12 | 225.44 | 0 | 2.25 | 45.81 |
| 13 | 317.90 | 0 | 3.18 | 43.23 |
| 14 | 443.19 | 0 | 4.43 | 40.74 |
| 15 | 611.12 | 0 | 6.11 | 38.33 |
| 16 | 833.74 | 0 | 8.34 | 36.00 |
| 17 | 1125.8 | 0 | 11.3 | 33.75 |
| 18 | 1505.2 | 0 | 15.1 | 31.57 |
| 19 | 1993.2 | 0 | 19.9 | 29.46 |
| 20 | 2614.9 | 0 | 26.2 | 27.43 |
| 21 | 3399.8 | 0 | 34.0 | 25.46 |
| 22 | 4382.1 | 0 | 43.8 | 23.56 |
| 23 | 5600.9 | 0 | 56.0 | 21.72 |
| 24 | 7100.7 | 0 | 71.0 | 19.94 |
| 25 | 8931.8 | 0 | 89.3 | 18.22 |
| 26 | 11150 | 0 | 111 | 16.55 |
| 27 | 13817 | 0 | 138 | 14.94 |
| 28 | 17001 | 0 | 170 | 13.39 |
| 29 | 20776 | 0 | 208 | 11.88 |
| 30 | 23967 | 0.01253 | 252 | 10.43 |
| 31 | 25528 | 0.04887 | 305 | 9.01 |

| | | | | |
|---|---|---|---|---|
| 32 | 25671 | 0.10724 | 365 | 7.65 |
| 33 | 24609 | 0.18455 | 433 | 6.37 |
| 34 | 22641 | 0.27461 | 505 | 5.23 |
| 35 | 20147 | 0.36914 | 576 | 4.24 |
| 36 | 17478 | 0.46103 | 642 | 3.42 |
| 37 | 14860 | 0.54623 | 702 | 2.75 |
| 38 | 12415 | 0.62305 | 755 | 2.20 |
| 39 | 10201 | 0.69099 | 802 | 1.75 |
| 40 | 8241.5 | 0.75016 | 843 | 1.38 |
| 41 | 6534.4 | 0.80110 | 877 | 1.08 |
| 42 | 5066.2 | 0.84453 | 906 | 0.84 |
| 43 | 3815.6 | 0.88127 | 931 | 0.63 |
| 44 | 2758.6 | 0.91217 | 952 | 0.47 |
| 45 | 1870.6 | 0.93803 | 969 | 0.33 |
| 46 | 1128.3 | 0.95958 | 984 | 0.22 |
| 47 | 510.48 | 0.97747 | 996 | 0.13 |
| 48 | 0. | 0.99223 | 1005 | 0.06 |
| 49 | 0. | 1 | 1013 | 0 |

**Table 2. Global land, area-average of standard deviation of 2-m temperature (1981-2000) ($^{\mathrm{O}}$C)**

| *Season* | *CRU2.0* | *CM2.1* | *CM3* |
|---|---|---|---|
| Annual | 0.567 | 0.768 | 0.677 |
| December-January-February | 1.197 | 1.639 | 1.391 |
| March-April-May | 0.919 | 1.280 | 1.178 |
| June-July-August | 0.675 | 1.037 | 0.878 |
| September-October-November | 0.820 | 1.127 | 0.925 |